Journal of Cosmology
and Astroparticle
Physics

PAPER

Cosmic recombination in the presence of primordial magnetic fields

To cite this article: Karsten Jedamzik *et al* JCAP03(2025)012

View the article online for updates and enhancements.

You may also like

- Adaptive and robust radiation therapy in the presence of drift
  Philip Allen Mar and Timothy C Y Chan
- Current and Future Constraints on Primordial Magnetic Fields
  Dylan R. Sutton, Chang Feng and Christian L. Reichardt
- Constraints on Primordial Magnetic Fields from High Redshift Stellar Mass Density
  Qile Zhang, Shang Li, Xiu-Hui Tan et al.

This content was downloaded from IP address 130.237.181.133 on 05/04/2025 at 19:11

Journal of Cosmology and Astroparticle Physics
An IOP and SISSA journal

Received: *December 7, 2024*
Accepted: *January 21, 2025*
Published: *March 6, 2025*

Cosmic recombination in the presence of primordial magnetic fields

Karsten Jedamzik,[a] **Tom Abel**[b,c,d] **and Yacine Ali-Haïmoud**[e]

[a]*Laboratoire Univers et Particules de Montpellier (LUPM),*
Université de Montpellier (UMR-5299) & CNRS,
Place Eugène Bataillon, Montpellier F-34095 Cedex 05, France
[b]*Kavli Institut for Particle Astrophysics and Cosmology, Stanford University,*
452 Lomita Mall, Stanford, CA 94305, U.S.A.
[c]*Department of Physics, Stanford University,*
382 Via Pueblo Mall, Stanford, CA 94305, U.S.A.
[d]*SLAC National Accelerator Laboratory,*
2575 Sand Hill Road, Menlo Park, CA 94025, U.S.A.
[e]*Center for Cosmology and Particle Physics, Department of Physics, New York University,*
New York, NY, U.S.A.
E-mail: karsten.jedamzik@umontpellier.fr, tabel@stanford.edu, yah2@nyu.edu

Abstract: Primordial magnetic fields (PMFs) may explain observations of magnetic fields on extragalactic scales. They are most cleanly constrained by measurements of cosmic microwave background radiation (CMB) anisotropies. Their effects on cosmic recombination may even be at the heart of the resolution of the Hubble tension. We present the most detailed analysis of the effects of PMFs on cosmic recombination to date. To this end we extend the public magneto-hydrodynamic code *ENZO* with a new cosmic recombination routine, Monte-Carlo simulations of Lyman-α photon transport, and a Compton drag term in the baryon momentum equation. The resulting code allows us, for the first time, to realistically predict the impact of PMFs on the cosmic ionization history and the clumping of baryons during cosmic recombination. Our results identify the importance of mixing of Lyman-α photons between overdense- and underdense- regions for small PMF strength. This mixing speeds up recombination beyond the speed-up due to clumping. We also investigate the effects of pecuilar flows on the recombination rate and find it to be small for small PMF strengths. For non-helical PMFs with a Batchelor spectrum we find a surprising dependency of results on ultra-violet magnetic modes. We further show that the increase in the ionization fraction at low redshift by hydrodynamic baryon heating due to PMF dissipation is completely compensated by the faster recombination from baryon clumping. The present study shall serve as a theoretical foundation for a future precise comparison of recombination with PMFs to CMB data.

Keywords: CMBR theory, primordial magnetic fields

ArXiv ePrint: 2312.11448

© 2025 IOP Publishing Ltd and Sissa Medialab.
All rights, including for text and data mining, AI training, and similar technologies, are reserved.

https://doi.org/10.1088/1475-7516/2025/03/012

Contents

1 Introduction

The local Universe seems to be permeated by magnetic fields in virtually all astrophysical environments observed [1]. Fields with large coherence scales of $\sim \mu$G magnitude are present in the Milky Way and other galaxies. Though details are not clear, these fields may be due to the action of a large-scale dynamo amplifying an initially small seed field [2]. Fields of similar strengths are also found in higher redshift galaxies [3, 4], where the fewer rotations those galaxies have undergone should make the dynamo less efficient. Magnetic fields of μG strengths are observed in clusters of galaxies and could be explained by outflows of the fields in galaxies within the cluster [5]. More difficult to explain are the fields of $\sim 50\,$nG strengths recently observed in filaments of the cosmic structure [6–8], in factor $\sim$ ten overdense regions, and it has been argued that a primordial origin may be the best explanation [9]. It came to a surprise in 2010 that observations of TeV and GeV γ-rays from blazars seem be most straightforwardly interpreted by an almost volume-filling cosmic magnetic field in the extragalactic medium, albeit of potentially weak strength $B_0 > 10^{-15}\,\mathrm{G}$ [10–15] (see also [16–22] for more recent observations). It may well be that all of these fields have a purely astrophysical origin, nevertheless, the community is far from a detailed understanding.

Alternatively, it has been proposed that magnetic fields may be a remnant of the early Universe. A plethora of magnetogenesis scenarios exist (for reviews cf. [1, 23, 24]). In case such a primordial magnetic field (hereafter, PMF) had ever been in equipartition with radiation, such as plausible during cosmic phase transitions (e.g. the electroweak transition), the smallest fraction $\sim 10^{-10}$ of this magnetic energy density surviving to the present, may be sufficient to explain all present day fields without dynamo action. In such scenarios the bulk of the magnetic energy density is indeed dissipated [25] with important details of such dissipation currently under debate [26–30], particularly in the non-helical case. Another possibility is that a PMF is generated right during inflation, in case conformal invariance of electro-magnetism is broken in the early Universe. In contrast to phase-transition generated magnetic fields, which have a very blue "Batchelor" spectrum [31, 32], inflationary produced fields have to be approximately scale-invariant and dissipation plays a much less important role.

It seems fair to say that the origin of magnetic fields in the present-day Universe is unknown, and further observations and theoretical work is needed. A seemingly clean argument in favor of PMFs would be their detection at very high redshift, before the epoch of structure formation, which is thought to provide the seed fields required by astrophysical generation mechanism.[1] An excellent probe could be the accurate observations of the spectrum of, and the anisotropies in the cosmic microwave background radiation (hereafter, CMB), which has already led to precision determination of cosmological parameters in a ΛCDM model, as well as its approximate confirmation. Indeed many authors have studied the effects of PMFs on the CMB. They considered anisotropic expansion [35], spectral y and μ distortions [36–38], anisotropies due to Alfven and slow magnetic waves [39–60], a changing ionization history due to plasma heating [38, 57, 61–64], extra polarization due to PMFs [41–43, 59, 65–73], as well as non-Gaussianity in bi- and tri-spectrum [57, 74–84]. Most works have not seen evidence for PMFs and have imposed upper limits in the comoving $\sim$nG range.[2] It is noted that these upper limits are much larger than the field strength $B_0 \sim 0.005\,\mathrm{nG}$ [85] required for clusters of galaxies to have an exclusively primordial origin.

More recently one particular effect of PMFs on CMB anisotropies has been identified. Independent on PMFs being of inflationary or phase transition origin, the small-scale part of the PMFs, dissipating around recombination, induces small-scale, non-linear density fluctuations in the baryons even for fairly weak $B_0 \sim 0.01$–$0.05\,\mathrm{nG}$ final present day field [86–88]. This is possible as on small scales the photons are free-streaming, and magnetic stresses may induce density fluctuations only opposed by the comparatively low baryon

---

[1] There are also a number of recent studies attempting to constrain approximately scale-invariant PMFs from the enhanced structure formation on small scales [33, 34].

[2] The exception here is the limit on PMFs of $B_0 < 0.05\,\mathrm{nG}$ [84] on inflationary fields from the non-Gaussianity in the tri-spectrum when the inflationary curvature mode is taken into account.

pressure. Recombination in such a “clumpy” Universe is sped up, due to high-density regions recombining earlier [89], thereby moving the peaks of the CMB to higher multipoles. This effect was confirmed in numerical MHD simulations and has been used to impose fairly stringent limits on PMFs [88].[3]

It has been subsequently shown that an earlier recombination due to PMFs and the associated baryon clumping, reduces the sound horizon and seems promising to relieve the Hubble tension [90, 91]. The Hubble tension is a $\sim 5\sigma$ tension between the present day Hubble constant H_0 inferred in the local Universe from Type 1A supernovae calibrated on Cepheids, and H_0 from CMB observations employing ΛCDM and a standard recombination history (see [92] for a review). Using the most recent Planck data, and three local H_0 determinations, a $3-4\sigma$ detection of baryon clumping before recombination was claimed, with an associated increase in H_0 to higher values [90]. When combing with other data sets, such as BAO, Type 1A supernovae and DES, the clumping detection significantly reduced. An analysis without the three local H_0 observations, using combinations of Planck data with high multipole CMB data ACT and SPT [93–95], did not show a clear detection of clumping. Thus CMB data only does not favor clumping but also does not rule it out to the degree that clumping could enhance the prediction for H_0. It is noted here that the existence of PMFs may be tested by direct observation of the remnant recombination radiation [96] and the formation of dark matter mini-halos [97].

All of the above analysis was performed using ad hoc three-zone baryon density probability distribution functions (pdfs) describing the clumping by one parameter b, the clumping factor, which is the variance of baryon density perturbations. Here the ionization history was computed by appropriately averaging the electron fraction of three independent regions with different baryon densities. Though such models may be good for a first description of clumping, they are insufficient for an accurate comparison between theory and observations, given the accuracy of current and future CMB data. In particular, one can show that the ionization history does not depend only on the baryon pdf, but on the evolution of baryon density of each gas element. In realistic scenarios the baryon pdf also evolves, whereas in three-zone models it is simply assumed constant. Moreover, three-zone models may assume a very unrealistic baryon pdf. Finally, a direct connection between the change in ionization history due to PMFs and the present-day leftover PMF field is hard to accurately establish in three-zone models.

In this paper we wish to address these issues, in order to obtain as precise as possible predictions. Such a study can only be performed by resorting to a host of full three-dimensional MHD simulations, which include all effects known to date. In the course of our study we analyze other so far unnoted effects, such as the effect of peculiar motions on the Lyman-α photon escape rate, and the transport of Lyman-α photons between different regions. We find, that in particular the latter effect is of importance. The goal of the paper is to improve the study of PMFs during recombination significantly as a preparation for an accurate comparison of PMF theory with CMB data in a future publication.

The outline of the paper is as follows. In section 2 we discuss details of the numerical MHD simulations, the employed MHD solver, the physical effects included, and the newly written recombination routine. We then present results of a realistic baryon pdf. Section 3

---

[3] The study used an effective three zone model and employing older CMB data.

reviews standard recombination theory and presents results of a Monte-Carlo analysis of the propagation of Lyman-alpha photons during recombination. In section 4 we analyze the effects of Lyman-α photon mixing on the ionization history, presenting a new explicit expression for the recombination rate in the full-mixing limit. Section 5 presents results of MHD simulations of PMFs before, during, and after recombination. Particular emphasis is laid on non-helical PMFs with a Batchelor spectrum and the change of the global free electron fraction $X_e \equiv \langle n_e \rangle / \langle n_{\rm H} \rangle$ (i.e. the ratio of the average free-electron abdundance to the average abundance of hydrogen nuclei) compared to a non-magnetized Universe. In section 6 we discuss the combined effect of baryon clumping and hydrodynamic heating by PMF dissipation on X_e. Conclusions are drawn in section 7. In appendix A we present the details of our Lyman-α Monte-Carlo simulation. Appendix B briefly describes helium recombination. Appendix C presents a numerical convergence study.

2 Numerical simulations of compressible MHD in the expanding Universe

2.1 Physical problem to be solved

In this paper we want solve the following problem. We assume a Gaussian-distributed primordial magnetic field $\mathbf{B}_{\rm prim} = \mathbf{B}(t \to 0)$. We then want to follow the time evolution of the magnetic field $\mathbf{B}$, coupled to the evolution of baryon density and peculiar velocity fields, ρ_b and $\mathbf{v}$, respectively. The MHD equations in an expanding Universe are given in refs. [25, 98]. Here we complement them by including photon drag on baryons, assuming photons to be free-streaming (i.e. have a mean-free path much larger than the scales of interest) thus uniform on the small scales of interest. We moreover neglect gravitational potentials, since we are interested in scales much smaller than the baryon Jeans scale. The equations to be solved are therefore

$$a\ \partial_t(a^3\rho_b) + \nabla\cdot(a^3\rho_b\mathbf{v}) = 0, \tag{2.1}$$

$$\partial_t(a\mathbf{v}) + (\mathbf{v}\cdot\nabla)\mathbf{v} + \alpha\ a\ \mathbf{v} = -\frac{\nabla(c_s^2\rho_b)}{\rho_b} + \frac{\mathbf{B}\times(\nabla\times\mathbf{B})}{4\pi\rho_b}, \tag{2.2}$$

$$\partial_t(a^2\mathbf{B}) = a\nabla\times(\mathbf{v}\times\mathbf{B}), \tag{2.3}$$

where all gradients are comoving, baryon velocity is in the CMB rest frame, and a is the scale factor, whose time evolution is given by $\dot{a}/a = H$, where H is the Hubble rate. Note that the equation for the magnetic field does not account for the Biermann-battery effect, which is relevant at much later times than of interest here [99, 100]. In the Euler equation (2.2), the (spatially-varying) baryon sound speed is

$$c_s^2 = \frac{n_{\rm tot}}{\rho_b}T_b \equiv \frac{n_{\rm H}(1+x_e)+n_{\rm He}}{\rho_b}T_b, \tag{2.4}$$

where T_b is the baryon temperature, $x_e \equiv n_e/n_{\rm H}$ is the (spatially-varying) free-electron fraction, with n_e the electron density and $n_{\rm H} = n_p + n_{H^0}$ the sum of proton and neutral hydrogen density, and $n_{\rm He} \approx 0.08\, n_{\rm H}$ is the total helium density, in both neutral and ionized forms. Even though photons are free-streaming, it is well known that in this limit the abundant photons still play an important role, as they induce a drag force on the baryons [89] proportional to the drag rate α, given by

$$\alpha = \frac{4}{3}\frac{n_e \sigma_{\rm Th} \rho_\gamma}{\rho_b}, \tag{2.5}$$

where $\sigma_{\rm Th}$ is the Thomson cross section, ρ_γ is the (uniform) photon energy density and m_p the proton mass. Before recombination $\alpha \gg H$ so photon drag forces the MHD evolution in the viscous regime, i.e. with Reynolds number of order unity. After recombination, the MHD evolution becomes turbulent.

We see that the MHD equations must be complemented by an evolution equation for the local ionization fraction x_e, relevant to both photon drag and baryon pressure. The evolution of x_e takes the following form:

$$\partial_t x_e + a^{-1}\mathbf{v}\cdot\nabla x_e = \frac{\dot{n}_e|_{\rm rec}}{n_{\rm H}}, \tag{2.6}$$

where $\dot{n}_e|_{\rm rec}$ is the (local) rate of change of free-electron density due to cosmological recombination, which we will discuss in more detail in the following sections. The most relevant quantity for CMB anisotropies is the *global* free-electron fraction X_e, defined as

$$X_e \equiv \frac{\langle n_e \rangle}{\langle n_{\rm H} \rangle} = \frac{\langle n_{\rm H} x_e \rangle}{\langle n_{\rm H} \rangle} = \frac{\langle \rho_b x_e \rangle}{\langle \rho_b \rangle}, \tag{2.7}$$

where $\langle \ldots \rangle$ denotes a spatial average. Accurately computing the effect of PMFs on X_e is one of the main goals of this work.

Though the baryon temperature T_b is to excellent approximation given by the CMB temperature $T_{\rm CMB}$ due to Thomson scattering for redshifts $z \gtrsim 1000$, it may deviate at lower redshifts. In particular, T_b may exceed $T_{\rm CMB}$ due to the energy released into the plasma by magnetic field dissipation [61]. The evolution of the local baryon temperature is governed by the following equation

$$\frac{dT_b}{dt} = \frac{2}{3}\frac{d\rho_b/dt}{\rho_b} + \frac{8\sigma_{Th} x_e n_{\rm H} \rho_\gamma}{3 m_e c n_{\rm tot}}(T_{\rm CMB} - T_b) + \frac{2\Gamma}{3 n_{\rm tot}}\,, \tag{2.8}$$

where the terms on the r.h.s. are due to adiabatic cooling/heating, CMB cooling/heating, and heating due to magnetic field dissipation, with Γ the volumetric heating rate. We will discuss Γ and the effects of this dissipation in section 6.

2.2 Numerical implementation

For the numerical simulations of PMFs before, during and after recombination we used the publicly available code *ENZO* [101]. We chose the MUSCL solvers with Dedner divergence cleaning described in [102]. Through rescaling all physical quantities by appropriate powers of the scale factor a, the MHD equations given above can be reformulated as the MHD equations in a Minkowski, static metric, with an additional drag term proportional to the Hubble rate. The Minkowski metric is chosen to coincide with the CMB rest frame. Specifically, we defined the rescaled variables

$$d\tilde{t} \equiv a^{-3/2}dt, \qquad \tilde{\rho}_b \equiv a^3 \rho_b, \qquad \tilde{\mathbf{v}} \equiv a^{1/2}\mathbf{v}, \qquad \tilde{\mathbf{B}} \equiv a^2 \mathbf{B}. \tag{2.9}$$

In terms of these variables, the MHD equations become

$$\frac{\partial \tilde{\rho}_b}{\partial \tilde{t}} + \nabla \cdot (\tilde{\rho}_b \tilde{\mathbf{v}}) = 0, \tag{2.10}$$

$$\frac{\partial \tilde{\mathbf{v}}}{\partial \tilde{t}} + (\tilde{\mathbf{v}} \cdot \nabla)\tilde{\mathbf{v}} + \left(\tilde{\alpha} + \frac{\tilde{H}}{2}\right)\tilde{\mathbf{v}} = -\frac{\nabla(\tilde{c}_s^2 \tilde{\rho}_b)}{\tilde{\rho}_b} - \frac{\tilde{\mathbf{B}} \times (\nabla \times \tilde{\mathbf{B}})}{4\pi \tilde{\rho}_b}, \tag{2.11}$$

$$\frac{\partial \tilde{\mathbf{B}}}{\partial \tilde{t}} = \nabla \times (\tilde{\mathbf{v}} \times \tilde{\mathbf{B}}), \tag{2.12}$$

where we have defined the rescaled sound speed, photon drag rate and expansion rate as

$$\tilde{c}_s \equiv a^{1/2} c_s, \qquad \tilde{\alpha} \equiv a^{3/2} \alpha, \qquad \tilde{H} \equiv a^{3/2} H. \tag{2.13}$$

For details the reader is referred to appendix B of [25]. The rescaling induces only one extra Hubble redshift term in the Euler equation, such that standard MHD codes in Minkowski space may be used when this term is included. It is noted that this rescaling may be applied during matter domination as well as radiation domination. As $T_b = T_{\rm CMB} \propto 1/a$ for $z \gtrsim 1000$, up to the dependence on x_e we have $c_s \propto 1/a^{1/2}$ which implies that $\tilde{c}_s$ is approximately constant. Nevertheless, $\tilde{c}_s$ drops by an approximate factor $1/\sqrt{2}$ during recombination due to the factor two smaller total particle number density when $x_e \to 0$.

In the rescaled variables, the free-electron fraction x_e evolves according to

$$\frac{\partial x_e}{\partial \tilde{t}} + \tilde{\mathbf{v}} \cdot \nabla x_e = a^{3/2} \frac{\dot{n}_e|_{\rm rec}}{n_{\rm H}}, \qquad \tilde{n}_{\rm H} \equiv a^3 n_{\rm H}. \tag{2.14}$$

To evolve x_e, we coupled the MHD simulations to a "chemical" solver which computes the abundances of singly ionised hydrogen and helium at each time step. The existing chemistry solver in *ENZO* [103] was optimized for non-equilibrium gas chemistry in the coronal limit [104] and is not suited for this study. We instead developed a new routine using a 6th order Runge-Kutta solver. We will discuss the recombination rate $\dot{n}_e|_{\rm rec}$ in great detail in sections 3 and 4, but in a nutshell, we include the most relevant processes during cosmological recombination and develop a new analytic result valid in the limit of scales much smaller than the mixing length of Lyman-α photons. We checked that our routine reaches 0.5–1.5% accuracy in comparison with Recfast [105] when computing recombination in a homogeneous Universe. Our routine does not, however, reach the sub-percent accuracy of state-of-the art cosmological recombination codes HYREC [106, 107] and COSMOREC [108], which include many other physical effects. As we will see, PMFs may easily change the free-electron fraction at the $\sim$20% level, and such an extreme accuracy is therefore not required for our purposes.

Let us emphasize that our implementation of recombination within the MHD simulations is an important novel aspect of this work, which goes well beyond the "three-zone model" implementations of past works, as we will discuss again later.

2.3 Results

All MHD simulations in this paper use default cosmological values of $h = 0.67$, $\Omega_b h^2 = 0.0224$, $\Omega_c h^2 = 0.12$, and $Y_p = 0.24$ for Hubble parameter, baryon density, CDM density, and helium mass fraction, respectively. In figure 1 results of a numerical simulation of a PMF

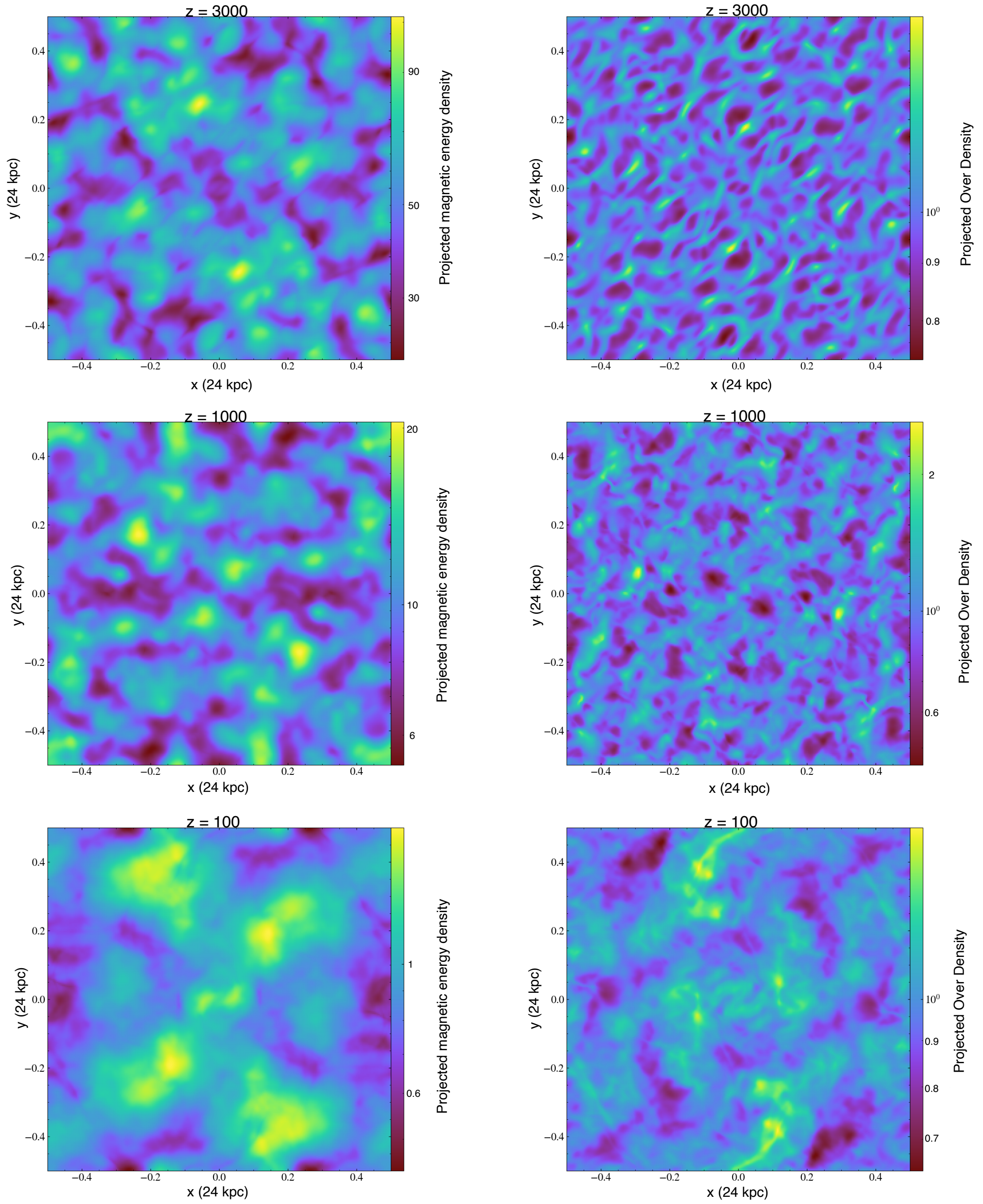

Figure 1. Two dimensional visualisations of the evolution of a PMF and the generated baryon density fluctuations in a 256^3 numerical MHD simulation of a non-helical PMF with Batchelor spectrum. Initial conditions at redshift $z = 4500$ were chosen as $V_{A,\rm rms} = 12c_s$ (i.e. comoving $0.526\,$nG) and vanishing density baryon fluctuations. The left panels show the projected $V^2_{A,\rm rms}$ whereas the right panels show the projected baryon overdensity $\Delta \equiv \rho_b/\langle\rho_b\rangle$ at three different redshifts $z = 3000$, 1000 and 100.

in a comoving $(24\,\text{kpc})^3$ box with resolution 256^3 are shown. In particular, the left panels show projected magnetic energy density at redshifts $z = 3000$, $z = 1000$, and $z = 100$, respectively, whereas the right panels show projected baryon overdensity $\Delta \equiv \rho_b/\langle\rho_b\rangle$ for the same redhifts. As initial conditions we chose a particular random configuration of a non-helical PMF with Batchelor spectrum

$$B(L) \sim L^{-5/2} \tag{2.15}$$

where L is length scale.[4] All modes with wavelength in the range $24\,\text{kpc} \geq \lambda \geq 3\,\text{kpc}$ were excited. The *rms* magnetic field strength in the simulation box has been normalized to $\tilde{B}_{\text{rms}} = 0.525\,\text{nG}$ comoving. This corresponds to an Alfven velocity twelve times as large as the speed of sound of singly ionized hydrogen and helium.[5] The simulation started at redshift $z = 4500$ with vanishing peculiar flows and uniform baryon density. Note that such initial conditions are very realistic. At early times when the photon mean free path $l_\gamma < L$, the effective speed of sound is large, $c_s = c/\sqrt{3}$, such that the fluid is incompressible and no substantial density fluctuations can be generated by relatively weak PMFs. When $l_\gamma \sim L$ photon dissipation is so strong that all pre-existing peculiar velocities will be erased. Only when $l_\gamma \gg L$ at lower redshift will magnetic stresses slowly be able to accelerate the fluid and build up density perturbations. For details of the evolution of PMFs in the early Universe the reader is referred to [25].

It is seen that by redshift $z = 3000$ the PMF has generated slightly non-linear density fluctuations on $\sim$ kpc scales. These overdensities seem to follow a filamentary structure. At redshift $z = 1000$, close to the maximum clumping produced in baryons, structures appear more fuzzy. This is due to the fluid leaving the viscous regime and transitioning into turbulence, due to the drop of electron density and the associated significant reduction of drag force. By redshift $z = 100$, when the clumping has significantly diminished, structures are even more fuzzy. At all three redshifts magnetic structures are more extended.

In figure 2 the evolution of comoving magnetic energy density, root-mean-square velocity, and clumping factor

$$b \equiv \frac{\langle\rho_b^2\rangle - \langle\rho_b\rangle^2}{\langle\rho_b\rangle^2} \tag{2.16}$$

are shown for this simulation. During the freely decaying evolution of the PMF the magnetic energy density is reduced by more than two orders of magnitude, leading to a final comoving rms field of $B_0 \approx 4.38 \times 10^{-2}\,\text{nG}$. Here the most rapid reduction occurs right around recombination, as dissipation which could not occur before due to the large photon drag

---

[4] Eq. (2.15) should be taken illustrative, meaning that the rms magnetic field strength when smoothed over L scales as $L^{-5/2}$. In praxis, to assure a divergence-free field $\nabla\mathbf{B} = \mathbf{0}$, the Fourier modes of the vector potential $\mathbf{A}$ with $\mathbf{B} = \nabla \times \mathbf{A}$ are excited with random amplitudes drawn from a Gaussian with width $\sigma_k \sim (k/k_0)^{5/2-3/2-1}$, where k is wavevector and k_0 a reference scale. Here the exponent $-3/2$ stems from phase space, i.e. $\langle B^2\rangle = k^3\langle\tilde{B}_k^2\rangle$ where $\tilde{B}_k$ is the Fourier amplitude, and the exponent -1 from the relationship between $\tilde{\mathbf{B}}_\mathbf{k} = \mathbf{k} \times \tilde{\mathbf{A}}$. Finally, one can show that a completely non-helical field is attained when setting all phases to zero in the Fourier decomposition.

[5] The speed of sound of singly ionized hydrogen and helium and the Alfven velocity at redshift $z = 1090$ are $c_s \approx 6.33\,\text{km/s}$ and $\text{v}_A = 4.34\,\text{km/s}[B_0/(0.03\,\text{nG})]$, respectively.

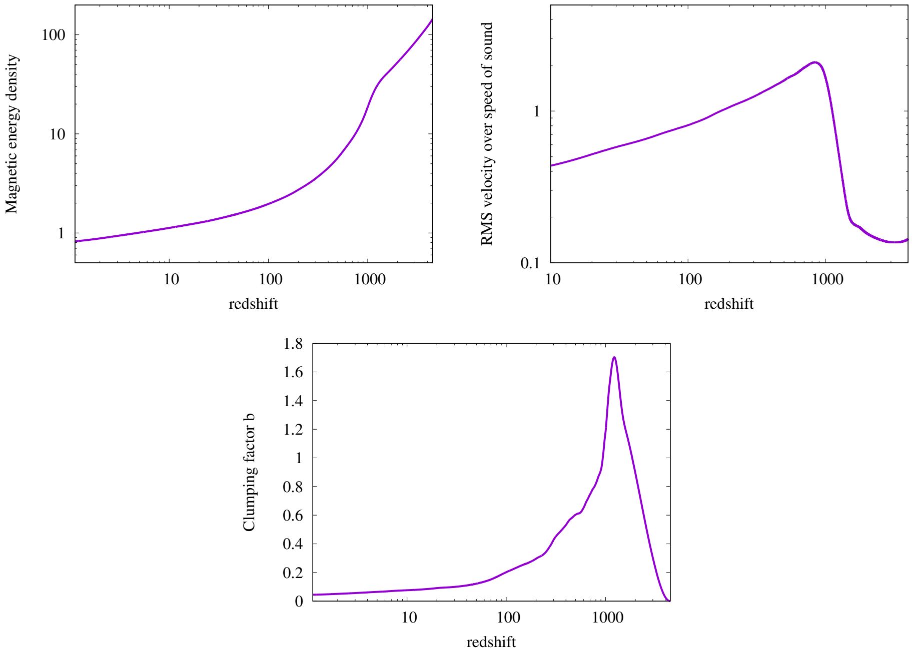

Figure 2. Redshift evolution of the comoving magnetic energy density $\epsilon_B = \tilde{B}^2_{\rm rms}/8\pi$, normalized to unity for $\tilde{B}_{\rm rms} = 4.38 \times 10^{-2}\,$nG (*top*), of the root-mean-square velocity over the speed of sound (*middle*), and of the baryon clumping factor b given in eq. (2.16) (*bottom*). Baryon density fluctuations are generated before recombination by the Lorentz force of the stochastic magnetic field. All quantities are evaluated for the numerical simulation shown in figure 1.

occurs when the fluid becomes turbulent. One may also observe the transition from viscous MHD to turbulent MHD by the increase of the root-mean-square velocity from subsonic values to slightly supersonic values during recombination. The PMF evolution time scale during recombination is thus not governed by the Hubble time, as during most other periods of the early Universe, but the shorter time scale of change in X_e. It is noted that even after recombination there is still some further decay. Simple analytic estimates [25] predict only logarithmic decay after recombination, but since the redshift range between recombination and the present is substantial, even logarithmic decay is still notable. The clumping factor of the baryons increases from zero to a maximum of $b \approx 1.7$ at redshift $z \approx 1250$ to then decrease to much lower values $b \approx 0.1$ at redshift $z \approx 10$. Due to the reduction of the speed of sound and the beginning of turbulent evolution right at recombination, clumping quickly increases due to magnetic stresses and then decreases due to baryonic pressure forces at recombination. The box size employed is such as to have the maximum effect at recombination, in order to induce the maximum change in ionisation history ΔX_e observable by the CMB anisotropies. Much smaller modes (simulation boxes) would induce the peak in b at higher redshifts, whereas much large modes would induce a peak in b at lower redshifts. We discuss this point further in section 5.2.

The left panel of figure 3 shows the pdf of baryon overdensity $P(\Delta)$ for a large number of redshifts. Red lines are for the redshift range $z = 4400$–1500 with the pdf becoming continuously harder, while green lines are for the redshift range $z = 1000$–10 with the pdf becoming softer again. At the peak of clumping a small fraction of volume $\sim 10^{-3}$ exists at extreme overdensities of $\Delta > 10$, while most of the volume is at $\Delta \approx 0.2$. The effects of PMFs on the baryons even for a final magnetic field strength as low as $\sim 0.05\,\mathrm{nG}$ are thus quite drastic. We note that those trends are not so well observed in figure 1, as there projected density is shown. The existence of very high-density zones poses a problem for the computation of the clumping factor. As we show in appendix B, in order to correctly resolve these high-density regions one needs very high resolution or adaptive mesh. The computed clumping factor b increases with resolution. However, also shown in appendix B is that the quantity which is really of interest, the ionization fraction X_e, converges even at lower resolutions. In three zone models a classification of the density fluctuations by b was employed. In realistic MHD simulations as performed here, the clumping factor should not really be used as a quantitative measure to obtain the connection between X_e and PMF strength B_0.

For comparison, "three-zone models" used in previous analyses assume an unrealistic PDF $P(\Delta) = \sum_{i=1}^{3} f_V^i\ \delta_{\mathrm{D}}(\Delta - \Delta_i)$, where the three overdensities Δ_i and volume-filling fractions f_V^i are constant in time, and satisfy $\sum_i f_V^i = 1 = \sum_i f_V^i \Delta_i$, and $\sum_i f_V^i \Delta_i^2 = 1 + b$. Here b is the clumping factor. This problem is underconstrained, so different models (M1, M2, etc...) make some extra ad-hoc assumptions to fix all six parameters $\{f_i, \Delta_i\}$. In the right panel of figure 3 we compare the numerically-obtained pdf of baryon density at $z = 1500$ to the M1 three-zone model with the same clumping factor $b = 1.28$. It is seen that the M1 model gives a particularly poor representation of the baryon pdf. The same holds for the M2 model. Both predict a much larger fraction of baryons at $\Delta > 1$ and a lower fraction of underdense regions than the simulations. We thus suspect that three-zone models overestimate the effect on ΔX_e, or vice versa, for a similar ΔX_e much larger clumping factors will occur in the realistic case, with a significant fraction of the contribution to the clumping factor from very high-density regions.

3 Lyman-α photon transport during recombination

In what follows we give a brief review of cosmological recombination and motivate the need for a Monte-Carlo computation of Lyman-α photon transport in an inhomogeneous Universe. We focus on Hydrogen recombination, which is most relevant to the MHD evolution (during the second Helium recombination, x_e is always in the range $(1, 1.08)$, regardless of the details of helium recombination), as well as to CMB anisotropies. For completeness, we briefly describe our simplified model for Helium recombination in appendix B.

3.1 Review of standard hydrogen recombination

3.1.1 The standard effective 3-level atom model

We assume that helium has fully recombined by the time hydrogen recombination starts, which is a very accurate approximation (see e.g. ref. [109]). As a consequence the abundances of free electrons and protons are equal by charge neutrality, $n_e = n_p$. We denote by n_{1s} the abundance of neutral hydrogen in its ground state, which to excellent accuracy is equal to the total abundance of neutral hydrogen, $n_{1s} \approx n_{H^0} = n_{\mathrm{H}} - n_e$, where n_{H} is the total abundance of hydrogen, ionized and neutral. To simplify the calculation, we assume that angular

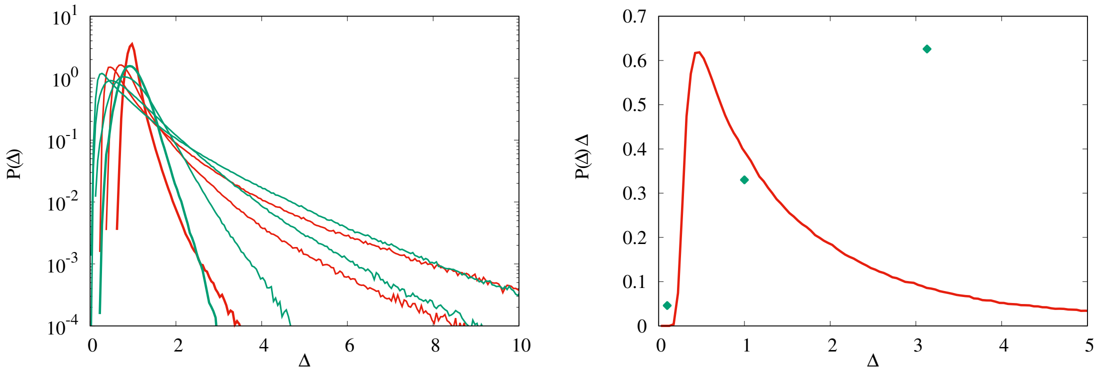

Figure 3. *Left*: probability $P(\Delta)$ to find a volume element at density between Δ and $\Delta + d\Delta$, where $\Delta \equiv \rho_b/\langle\rho_b\rangle$. The redshift evolution for the numerical simulation shown in figure 1 at $z = 4000$, 3000, 2000, 1000, 500, 100 and 10 is shown. $P(\Delta)$ is shown by red (green) lines before (after) the maximum of the clumping factor occurs at $z_{\rm max} \approx 1250$. The lines for $P(\Delta)$ at redshifts $z = 4000$ and $z = 10$ are slightly thicker. For $z > z_{\rm max}$ the maximum moves to lower densities and very high density regions get more and more probable, whereas for lower redshifts $z < z_{\rm max}$ the maximum moves to higher densities and very high density regions get less and less probable. *Right*: the probability $P(\Delta)\Delta$ to find a baryon at density between Δ and $\Delta + {\rm d}\Delta$ at redshift $z = 1500$, compared with the analogous quantity $f_V^i \Delta_i$ for the M1 three-zone model at the same clumping factor $b = 1.28$, shown with green dots. This illustrates that three zone models do not capture the baryon probability function correctly.

momentum substates within a given energy shell are in statistical equilibrium, so that, in particular, the abundance of hydrogen in the $2p$ and $2s$ states are related through $n_{2p} = 3n_{2s}$.

Direct recombinations to the ground state are highly inefficient due to the very short mean-free-path of Lyman-continuum photons. As a consequence, recombination proceeds through the excited states, with a rate given by [110]

$$\dot{n}_e|_{\rm rec} = -\alpha_e n_e^2 + \beta_e n_{2s}, \tag{3.1}$$

where α_e is the case-B radiative-recombination coefficient and β_e is the corresponding photoionization rate per atom in the $2s$ state.[6] Note that instead of the exact effective recombination coefficient $\mathcal{A}_B(T_\gamma, T_b)$ computed in ref. [106], where T_γ and T_b are the photon and baryon temperatures, respectively, we use the RecFast approximation [105, 111, 112] $\alpha_e(T_b) = 1.14\ \mathcal{A}_B(T_\gamma = 0, T_b)$, where $\mathcal{A}_B(0, T_b)$ is obtained from ref. [113], and obtain β_e by detailed balance.

This equation must be complemented by an evolution equation for the abundance of excited hydrogen $n_2 = n_{2s} + n_{2p} = 4n_{2s}$. It evolves due to three processes: radiative recombinations (and the corresponding photoionization), two-photon transitions from the $2s$ state, and Lyman-α transitions from the $2p$ state:

$$\dot{n}_2 = -\dot{n}_e|_{\rm rec} + \dot{n}_{2s}|_{2\gamma} + \dot{n}_{2p}|_{{\rm Ly}\alpha}. \tag{3.2}$$

---

[6] We choose to write all the rates in terms of the abundance of hydrogen in the $2s$ state, instead of the total abundance of excited hydrogen $n_2 = 4n_{2s}$. Therefore, β_e is 4 times the photoionization rate per atom in the $n = 2$ state.

Up to small corrections, the two-photon term is

$$\dot{n}_{2s}|_{2\gamma} = -\Lambda_{2\gamma}\left(n_{2s} - n_{1s}e^{-E_\alpha/T_\gamma}\right), \tag{3.3}$$

where $\Lambda_{2\gamma} \approx 8.22\,\mathrm{s}^{-1}$ is the $2s \to 1s$ two-photon spontaneous decay rate and $E_\alpha = 10.2\,\mathrm{eV}$ is the energy between the ground and first excited state.

Naively, the net decay rate in the Lyman-alpha transition would take a similar form, with the much larger $2p \to 1s$ spontaneous decay rate $A_{2p,1s} \approx 6.3 \times 10^8\,\mathrm{s}^{-1}$. However, because the Lyman-α transition is optically thick, only a small fraction of emitted photons redshift out of the line and escape reabsorption. In the Sobolev approximation, this fraction is $P_{\rm esc} \approx 8\pi H/(3\lambda_\alpha^3 n_{1s} A_{2p,1s}) \ll 1$, where λ_α is the Lyman-α wavelength and H is the expansion rate. The net decay rate in the Lyman-α transition is thus

$$\begin{aligned} \dot{n}_{2p}|_{\mathrm{Ly}\alpha} &= -P_{\rm esc}A_{2p,1s}\left(n_{2p} - 3n_{1s}e^{-E_\alpha/T_\gamma}\right) \\ &= R_\alpha\left(n_{2s} - n_{1s}e^{-E_\alpha/T_\gamma}\right), \end{aligned} \tag{3.4}$$

where

$$R_\alpha = 3P_{\rm esc}A_{2p,1s} = \frac{8\pi H}{\lambda_\alpha^3 n_{1s}}. \tag{3.5}$$

In practice, we may solve for n_{2s} in the quasi-steady state approximation, taking advantage of the very short timescale for transitions into and out of the excited states relative to the expansion rate:

$$\dot{n}_{2s} \approx 0 = \alpha_e n_e^2 - \beta_e n_{2s} - (\Lambda_{2\gamma} + R_\alpha)\left(n_{2s} - n_{1s}e^{-E_\alpha/T_\gamma}\right), \tag{3.6}$$

implying

$$n_{2s} = \frac{\alpha_e n_e^2 + (\Lambda_{2\gamma} + R_\alpha)n_{1s}e^{-E_\alpha/T_\gamma}}{\beta_e + \Lambda_{2\gamma} + R_\alpha}. \tag{3.7}$$

Inserting this result into eq. (3.1), one obtains the following net rate of recombinations:

$$\dot{n}_e|_{\rm rec} = -C\left(\alpha_e n_e^2 - \beta_e n_{1s}e^{-E_\alpha/T_\gamma}\right), \tag{3.8}$$

where the dimensionless parameter C is the famous Peebles suppression factor

$$C = \frac{\Lambda_{2\gamma} + R_\alpha}{\beta_e + \Lambda_{2\gamma} + R_\alpha}, \tag{3.9}$$

which quantifies the efficiency of net transitions to the ground state (accounting for the suppression of Lyman-α transitions due to their large optical depth) relative to the total net rate of transitions out of the excited state. The Peebles C factor is much less than unity for $z \gtrsim 1000$ (of order $C \sim 10^{-2}$ near the peak of the visibility function at $z \approx 1100$), and becomes close to unity for $z \lesssim 800$.

In the absence of large inhomogeneities, the background ionization history is obtained by solving eq. (3.8) with the background abundances $n_e = \langle n_e \rangle$ and $n_{1s} = \langle n_{1s} \rangle$.

3.1.2 Perturbed recombination in the no-mixing limit

The generalization of the recombination rate to a perturbed Universe is well-known in the limit that the characteristic distance D_α traveled by Lyman-α photons before re-absorption (as opposed to merely scattering) is much shorter than the length scale λ of perturbations of interest [114, 115]. In that case, recombination is entirely local.[7] The local net recombination rate is then still given by eq. (3.8), where n_e and n_{1s} are now the local ionized and neutral hydrogen densities, and with a modified net rate of Lyman-α loss obtained from substituting $H \to H + \frac{1}{3}\nabla \cdot \mathbf{v}$ in eq. (3.5), where $\nabla \cdot \mathbf{v}$ is the local divergence of baryon peculiar velocities. The latter substitution accounts for the enhanced (or decreased) redshifting of Lyman-α photons out of resonance for diverging (or converging) local bulk flows. Note that this substitution is exact (in the limit that $D_\alpha \ll \lambda$) for large diverging local bulk flows with $\nabla \cdot \mathbf{v} > 0$, as long as the local optical depth for true Lyman-α absorption, inversely proportional to $(H + \nabla \cdot \mathbf{v}/3)$, remains large, which in practice means as long $\nabla \cdot \mathbf{v}/3 \lesssim 10^4 H$. However, for converging local bulk flows with $\nabla \cdot \mathbf{v} < 0$, the expression only holds as long as $\nabla \cdot \mathbf{v}/3 > -H$, and special care should be given for more negative local velocity divergence.

In the case of non-linear baryon perturbations sourced by primordial magnetic fields of the characteristic strengths we consider in this paper, we find root-mean-square values for the local divergence of peculiar flows of $(\nabla \cdot \mathbf{v})_{\rm rms} \sim 20H$, indicating that bulk flows could in principle have a *very* significant effect on the net rate of Lyman-α decays. However, the problem we consider is *not* within the $D_\alpha \ll \lambda$ limit: as we will see, D_α is of the same order or larger than $\lambda \approx 1\,\text{kpc}$, the typical magnetically induced velocity- and density- fluctuation length. As a consequence, recombination is no longer local, as different patches “communicate” through Lyman-α photons, and the net rate of recombination must be re-examined.

In the next subsection, we evaluate the typical distance D_α traveled by Lyman-α photons using Monte Carlo simulations.

3.2 Lyman-α mixing length from Monte Carlo simulations

In our Monte-Carlo simulations we inject Lyman-α photons into the plasma, and follow their evolution in physical and frequency space during the $\sim 10^5$–10^7 scattering events on neutral hydrogen, before reionzation by the CMBR black body of the excited $n = 2$ state and thus absorption of the Lyman-α photon. Photons which diffuse in frequency too far onto the red wing of the Lyman-α resonance line are likely lost by redshifting. Photons which “diffuse” too far in physical space are subject to different local physical conditions in $\nabla\mathbf{v}$ and density. The details of our Monte Carlo method are presented in appendix A.

Figure 4 shows the fractions $f_\alpha(D)$ of Lyman-α photons having traveled between creation and destruction further than distance D. In the top panel, we show this function for different redshifts, highlighting the fact that at lower redshifts Lyman-α photons travel further before being destroyed. This is due to the decrease in the photoionization rate by CMB photons β_e, whereas the Lyman-α de-excitation rate $A_{2p,1s}$ remains constant. It is seen that appreciable fractions of photons travel further than the typical comoving fluctuation length $\lambda \approx 1\,\text{kpc}$.

---

[7] This limit also requires the mean-free path of Lyman-continuum photons to be short relative to the scales of interest. This mean-free path is of order a comoving parsec [116], much smaller than the scales we consider here, so we need not consider the finite propagation of Lyman-continuum photons.

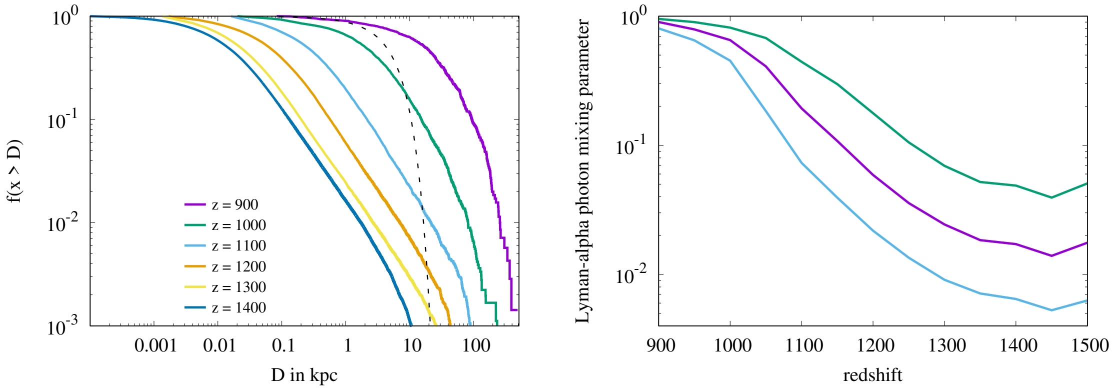

Figure 4. Fraction of Lyman-α photons which have traveled further than a given comoving distance D before being destroyed (i.e. absorbed followed by a photoionization or 2-photon decay). *Top*: this fraction is shown as a function of comoving distance D, for several discrete redshifts $900 \leq z \leq 1400$. The light dotted line shows the result for simple diffusion at redshift $z = 1100$, i.e. a Gaussian distribution with the same variance as that inferred from the realistic distribution. *Bottom*: this fraction, interpreted as a scale-dependent Lyman-α mixing fraction, is shown as a function of redshift, for comoving scales $D = 0.3$, 1 and 3 kpc, respectively, from top to bottom.

Figure 4 also shows by the dotted line the equivalent distribution at $z = 1100$, in case the propagation would be a diffusive random walk. It is seen that simple diffusion does not apply. As argued in ref. [116] the distribution is more like a blast wave. Most of the distance is covered during a few $\sim 10^3$ scattering events, when the Lyman-α photon is temporarily on the extreme red or blue wing of the line, as here the mean free path drastically increases (cf. figure 13). During the remainder of the $\sim 10^5$–10^7 scatterings, when the Lyman-α photons are in the core of the line, hardly any distance is covered.

As can be observed from the top panel of figure 4 Lyman-α photon mixing on $\sim$kpc scales is substantial but not complete, in particular at high redshifts. The bottom panel shows the evolution of $f_\alpha(D)$ with redshift, for three different scales, $D = 0.3$, 1, and 3 kpc, from top to bottom. This fraction can be interpreted as a "mixing fraction" for each length scale.

Figure 5 investigates the fraction of Lyman-α photons which is lost due to redshifting, as a function of bulk flows. Without bulk flows, in a Universe with cosmological parameters as inferred from the best-fit to the Planck data, the fraction of photons lost due to redshifting and lost due to two photon decay are $f_z(\mathrm{v} = 0) \approx 5 \times 10^{-3}$ and $f_{2\gamma} \approx 1.5 \times 10^{-2}$ at redshift $z \approx 1100$, respectively. In the presence of peculiar flows results are very dependent of the coherence scale λ of the flow. The yellow line shows result for $\lambda \gg D_\alpha$ and is in full agreement with the analytical result. However, for smaller λ the effect is much diminished as the Lyman-alpha photons alternatively travel through diverging and converging flows. For $\lambda = 0.1$ kpc the result of $f_z(\mathrm{v} = 0)$ is essentially recovered, whereas for $\lambda = 1$ kpc there is a small deviation from $f_z(\mathrm{v} = 0)$, with however a reduction for $\nabla \cdot \mathbf{v} < 0$ and an enhancement for $\nabla \cdot \mathbf{v} > 0$. In section 5 we perform MHD simulations for a variety of magnetic field strength. From these simulations we can infer at typical $\lambda \approx 0.1$ kpc and 1 kpc for PMFs with a Batchelor spectrum leading to a "final" field strength of 20 pG and 136 pG, respectively. We suspect therefore that for low final field strengths the effects of peculiar flows on the

Lyman-α escape rate should be negligible, whereas for much stronger PMFs, we expect an additional reduction of X_e due to peculiar flows. However, this latter field strength seems already ruled out if only the effect of clumping is taken into account [88].

It is our goal to obtain a very precise prediction of the average ionzation fraction X_e. To verify our suspicion that additional losses of Lyman-α photons due to bulk flows are negligible, we have indulged in a more elaborate Monte Carlo simulation of Lyman-α photon loss. In particular, we have used snapshots of the numerical simulations in order to have a realistic and detailed knowledge of the density- and velocity- distribution at a given redshift. We have then "emitted" Lyman-α photons from a great number of randomly chosen locations and followed their propagation in physical space and evolution of energy space. This allowed us to compute the *global* Lyman-α photon loss rate numerically[8] and compare it to the one in a Universe without peculiar bulk flows and fully mixed Lyman-α photons. Differences between these two global loss rates are due to two effects: bulk flows and the effect of partial Lyman-α mixing important at higher redshifts where D_α becomes relatively small. To isolate the two effects we ran our Monte-Carlo simulations with and without pecuilar flows. For a simulation with Batchelor spectrum leading to a final field of 20 pG we did find an enhancement of the loss reate by only a few percent, with the loss rate at the most important redshifts around recombination $z \sim 1100$ virtually identical. The enhancement of a few per cent was in almost equal parts due to bulk flows and partial Lyman-α photon mixing. By computing the changes in ionization history due to the small enhancement of Lyman-α photon loss in a homogeneous Universe (for simplicity) we could conclude that the relative change should be below the one per cent level for those field strengths not already ruled out. We conclude therefore that negelcting bulk flows and assuming full Lyman-α mixing introduces errors in X_e not larger than one per cent.

JCAP03(2025)012

4 Hydrogen recombination with Lyman-α photon mixing

In the previous section we have found that in an inhomogeneous Universe, with inhomogeneities on comoving kpc scales, Lyman-α photons of different regions may actually partially mix. We now investigate the effect on the average ionization fraction during recombination. Our work is mostly concerned with hydrogen recombination, and we briefly describe our approximate treatment of Helium recombination in appendix B.

4.1 Net Lyman-α transition rate in the full-mixing limit

4.1.1 General setup

In order to treat Lyman-α photon mixing, we must return to the first-principles derivation of the net decay rate in the Lyman-α transition. We will follow ref. [117].

At a fundamental level, the net decay rate depends on the photon occupation number $f_\nu(\hat{n})$ in the vicinity of the Lyman-α resonance, averaged over photon propagation directions

---

[8] In particular we evaluated the integral $(1/V)\int C\alpha_e n_e^2$ by Monte Carlo integration and compared it to the fully Lyman-α mixed (cf. section 4) result $(1/V)\, C^{\rm mix}\int \alpha_e n_e^2$ which was applied in the simulations.

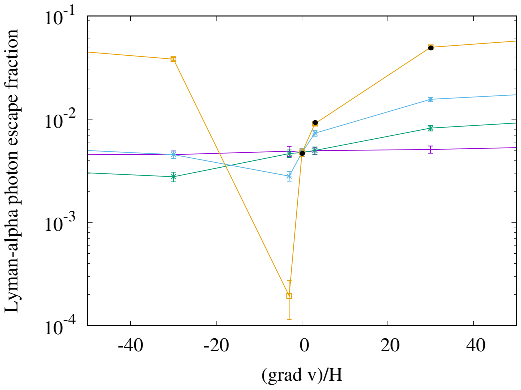

Figure 5. The fraction of Lyman-α photons lost due to redshifting as a function of the gradient of the bulk velocity over the Hubble constant $\nabla \cdot \mathbf{v}/H$. Results of the Monte-Carlo simulation are shown by dots with lines as a visual aid. The 3D simulation assumes a bulk flow of form $\mathrm{v}_b = \mathrm{v}_0 \sin(2\pi\, x/\lambda)$ in x-direction and photons are injected at $x = 0$. Purple, green, blue, and yellow dots are for comoving $\lambda = 0.1\,\mathrm{kpc}$ $\lambda = 1.\,\mathrm{kpc}$, $\lambda = 10\,\mathrm{kpc}$, and $\lambda = 1\,\mathrm{Mpc}$ respectively. The two black dots show the analytical result i.e. $H \to H + \nabla \mathbf{v}/3$, for coherent bulk flows on very large scales, illustrating agreement between the Monte-Carlo and the analytical result. The computation was performed at redshift $z = 1100$, the redshift of the approximate peak of the CMB visibility function.

$\hat{n}$ and integrated over the line profile $\phi(\nu)$:

$$\dot{n}_{2p}|_{\mathrm{Ly}\alpha} = -A_{2p,1s}\left[n_{2p} - 3n_{1s}\iint \frac{d^2\hat{n}}{4\pi}\, d\nu\ \phi(\nu) f_\nu(\hat{n})\right], \tag{4.1}$$

where the line profile integrates to unity, $\int d\nu\ \phi(\nu) = 1$. To obtain $\dot{n}_{1s}|_{\mathrm{Ly}\alpha}$, we must therefore solve the radiative transfer equation for $f_\nu(t, \vec{x}, \hat{n})$.

Near the Lyman-α resonance, photons may undergo resonant scattering events $\gamma_{\mathrm{Ly}\alpha} + \mathrm{H}(1s) \to \gamma'_{\mathrm{Ly}\alpha} + \mathrm{H}(1s)$, true absorption events $\gamma_{\mathrm{Ly}\alpha} + \gamma_{\mathrm{bb}} + \mathrm{H}(1s) \to \mathrm{H}^*$, where H^* is an excited (or ionized) atom in a s of d angular momentum state and γ_{bb} is a blackbody photon with energy corresponding to the $\mathrm{H}(2p) \to \mathrm{H}^*$ transition, or the reverse "true emission" process, see e.g. refs. [117, 118]. The radiative transfer equation then takes the form

$$\partial_t f_\nu + \hat{n} \cdot \nabla f_\nu - H\nu\ \partial_\nu f_\nu = \dot{f}_\nu|_{\mathrm{scat}} + \dot{f}_\nu|_{\mathrm{em,ab}}. \tag{4.2}$$

The timescale it takes a photon to redshift across the optically thick part of the line is much shorter than a Hubble time, and one may therefore solve this equation in the quasi-steady-state approximation, i.e. neglecting the partial time derivative $\partial_t f_\nu$.

Before describing the scattering and emission/absorption terms, we first define $p_{\mathrm{sc}} \equiv A_{2p,1s}/\Gamma_{2p}$, where Γ_{2p} is the total rate of all transitions out of the $2p$ state. The quantity p_{sc} is the probability that an atom in the $2p$ state decays to the ground state rather than be excited or ionized by a blackbody photon. We denote its complementary by $p_{\mathrm{ab}} = 1 - p_{\mathrm{sc}}$. These two probabilities only depend on photon temperature and are therefore nearly homogeneous.

The scattering term $\dot{f}_\nu|_{\mathrm{scat}}$ does not change photon number, and only changes photon direction and frequency. The latter effect is due to the thermal motions of scattering atoms. It is not essential to our derivation, and we shall therefore ignore atomic velocities as a first pass, and come back to this point at the end of the derivation. In that limit, resonant scattering simply changes photon propagation directions, while preserving the angle-integrated photon occupation number:

$$\int d^2\hat{n}\ \dot{f}_\nu|_{\rm scat}(\hat{n}) \approx 0. \tag{4.3}$$

The true emission/absorption term in eq. (4.2) is given by (see ref. [117] for a derivation, which is easily generalized to arbitrary angular dependence):

$$\dot{f}_\nu|_{\rm em,ab} = p_{\rm ab}\frac{3A_{2p,1s}}{8\pi\nu^2}\phi(\nu)\left(n_{1s}f_{\rm (em)} - n_{1s}f_\nu\right), \tag{4.4}$$

$$f_{\rm (em)} \equiv p_{\rm ab}^{-1}\left(\frac{n_{2p}}{3n_{1s}} - p_{\rm sc}\iint\frac{d^2\hat{n}}{4\pi}d\nu\ \phi(\nu)f_\nu(\hat{n})\right). \tag{4.5}$$

4.1.2 Net decay rate in the full-mixing limit

We now consider the limit in which the characteristic distance traveled by Lyman-α photons between emission and (true) absorption is much longer than the wavelength of perturbations of interest. In that case, we may assume that the photon occupation number is approximately isotropic and homogeneous, $f_\nu(t,\vec{x},\hat{n}) \approx \langle f_\nu\rangle$.

Inserting this approximation into the radiative transfer equation, and averaging over angles, we see that the gradient term $\hat{n}\cdot\nabla f_\nu$ and the scattering term (in the limit of negligible atomic motions) both drop out. Taking the spatial average of the equation (and recalling that we make the steady-state approximation and neglecting $\partial_t f_\nu$), we then obtain

$$\partial_\nu\langle f_\nu\rangle \approx \langle\tau_{\rm ab}\rangle\phi(\nu)\left[\langle f_\nu\rangle - f_{\rm (em)}^{\rm mix}\right], \tag{4.6}$$

where $\langle\tau_{\rm ab}\rangle$ is the average optical depth to true absorption,

$$\langle\tau_{\rm ab}\rangle = \frac{3A_{2p,1s}}{8\pi H\nu_\alpha^3}p_{\rm ab}\langle n_{1s}\rangle, \tag{4.7}$$

where we approximated $\nu \approx \nu_\alpha$, the resonant frequency, and we have moreover defined

$$f_{\rm (em)}^{\rm mix} \equiv \frac{\langle n_{1s}f_{\rm (em)}\rangle}{\langle n_{1s}\rangle} = p_{\rm ab}^{-1}\left(\frac{\langle n_{2p}\rangle}{3\langle n_{1s}\rangle} - p_{\rm sc}\int d\nu\ \phi(\nu)\langle f_\nu\rangle\right). \tag{4.8}$$

Equation (4.7) is a simple linear 1st-order ODE, to be solved under the boundary condition of thermal equilibrium $\langle f_\nu\rangle \to e^{-h\nu/T_\gamma} \approx e^{-E_\alpha/T_\gamma}$ at $\nu \to +\infty$ (neglecting feedback from higher-order lines, and again approximating $\nu \approx \nu_\alpha$ within the boundaries of the problem). It has the explicit solution

$$\langle f_\nu\rangle = f_{\rm (em)}^{\rm mix} + \left(e^{-E_\alpha/T_\gamma} - f_{\rm (em)}^{\rm mix}\right)\exp\left[-\langle\tau_{\rm ab}\rangle\int_\nu^\infty d\nu'\phi(\nu')\right]. \tag{4.9}$$

Integrating this equation over the line profile and using the definition of $f_{\rm (em)}^{\rm mix}$, eq. (4.8), we obtain, in the relevant limit that $\langle\tau_{\rm ab}\rangle \gg 1$,

$$\int d\nu\ \phi(\nu)\ \langle f_\nu\rangle \approx \frac{\langle n_{2p}\rangle}{3\langle n_{1s}\rangle} + \frac{p_{\rm ab}}{\langle\tau_{\rm ab}\rangle}\left(e^{-E_\alpha/T_\gamma} - \frac{\langle n_{2p}\rangle}{3\langle n_{1s}\rangle}\right). \tag{4.10}$$

JCAP03(2025)012

We are now in a position to compute the *local* net Lyman-α decay rate: it is given by eq. (4.1), where n_{2p} and n_{1s} are *local* abundances, but $f_\nu = \langle f_\nu \rangle$ is the homogeneous photon occupation number, that is,

$$\begin{aligned}\dot{n}_{2p}|_{\mathrm{Ly}\alpha} &= -A_{2p,1s}\left[n_{2p} - 3n_{1s}\int d\nu\ \phi(\nu)\langle f_\nu\rangle\right] \\ &= -R_\alpha^{\mathrm{mix}} n_{1s}\left[\frac{\langle n_{2s}\rangle}{\langle n_{1s}\rangle} - e^{-E_\alpha/T_\gamma}\right] - 3A_{2p,1s}\left[n_{2s} - n_{1s}\frac{\langle n_{2s}\rangle}{\langle n_{1s}\rangle}\right], \end{aligned} \tag{4.11}$$

where we substituted $n_{2p} = 3n_{2s}$ and we have defined

$$R_\alpha^{\mathrm{mix}} \equiv \frac{8\pi H}{\lambda_\alpha^3 \langle n_{1s}\rangle} = 1/\langle R_\alpha^{-1}\rangle. \tag{4.12}$$

We see that, in the limit that the baryon density is homogeneous, so that $n_{1s} = \langle n_{1s}\rangle$ and $n_{2s} = \langle n_{2s}\rangle$, this net decay rate reduces to eq. (3.4), as it should. However, in the presence of inhomogeneities, the net decay rate can be *significantly* different, especially due to the second term in the right-hand-side of eq. (4.11), given that $A_{2p,1s} \gg R_\alpha$.

4.1.3 Effect of diffusion and bulk flows

So far we have entirely neglected photon frequency diffusion due to resonant scattering off of thermally moving atoms, as well as the effect of bulk flows. The former effect is known to lead to $\mathcal{O}(4\%)$ corrections to the Lyman-α net decay rate at $z \approx 1100$, see e.g. ref. [119], and we expect that correctly incorporating them would lead to similar corrections in the full-mixing limit. Since Lyman-α photons scatter many times between emission and true absorption, for perturbations much smaller than the Lyman-α re-absorption length scale, they scatter off many patches with incoherent peculiar velocities. Hence, on small scales bulk flows act effectively as an additional contribution to thermal motions. Therefore we expect that, in the full mixing limit, baryon peculiar velocities v can be effectively incorporated by substituting $T_b \to T_b + m_p\langle \mathrm{v}^2\rangle/3 \approx T_b\left(1 + \langle \mathrm{v}^2\rangle/3c_s^2\right)$ in the resonant scattering diffusion operator, where we took the limit $X_e \ll 1$ in c_s^2. Assuming the effect of frequency diffusion scales linearly with T_b as long as it is perturbative, we expect bulk flows to start significantly affecting the net Lyman-α decay rate when $\langle \mathrm{v}^2\rangle/3c_s^2 \gtrsim 1/(4\%) \sim 25$, i.e. when $\langle \mathrm{v}^2\rangle^{1/2} \gtrsim 9c_s$.

4.2 Local recombination rate in the full mixing limit

To find the local recombination rate, we must again solve for the abundance of excited hydrogen in the steady-state approximation. Instead of eq. (3.6), we now have

$$\begin{aligned}0 \approx \dot{n}_{2s} &= \alpha_e n_e^2 - \beta_e n_{2s} - \Lambda_{2\gamma}\left(n_{2s} - n_{1s}e^{-E_\alpha/T_\gamma}\right) \\ &\quad - R_\alpha^{\mathrm{mix}} n_{1s}\left[\frac{\langle n_{2s}\rangle}{\langle n_{1s}\rangle} - e^{-E_\alpha/T_\gamma}\right] - A_{2p,1s}\left[n_{2s} - n_{1s}\frac{\langle n_{2s}\rangle}{\langle n_{1s}\rangle}\right]. \end{aligned} \tag{4.13}$$

We solve this equation in two steps. First, we take its spatial average. This eliminates the last term, and results in an equation for $\langle n_{2s}\rangle$ identical to eq. (3.6), with the substitutions $(n_e^2, n_{1s}, n_{2s}, R_\alpha) \to (\langle n_e^2\rangle, \langle n_{1s}\rangle, \langle n_{2s}\rangle, R_\alpha^{\mathrm{mix}})$ with solution therefore identical to eq. (3.7) with the same substitutions. Next, we solve the local quasi-steady state equation (4.13) for n_{2s}, given n_e^2, n_{1s} and their average values. In practice, given that $A_{2p,1s} \gg \beta_e, R_\alpha, \Lambda_{2\gamma}$, the solution is very well approximated by

$$n_{2s} \approx n_{1s} \frac{\langle n_{2s} \rangle}{\langle n_{1s} \rangle}. \tag{4.14}$$

We can now finally compute the local net recombination rate, $\dot{n}_e|_{\rm rec} = -(\alpha_e n_e^2 - \beta_e n_{2s})$, which, after substituting the solution for n_{2s}, becomes

$$\dot{n}_e|_{\rm rec} = -C^{\rm mix} \left(\alpha_e n_e^2 - \beta_e n_{1s} e^{-E_\alpha/T_\gamma} \right) - (1 - C^{\rm mix}) \alpha_e \left(n_e^2 - \frac{n_{1s}}{\langle n_{1s} \rangle} \langle n_e^2 \rangle \right), \tag{4.15}$$

where the full-mixing Peebles-C factor $C^{\rm mix}$ is given by eq. (3.9) with the substitution $R_\alpha \to R_\alpha^{\rm mix} = 1/\langle R_\alpha^{-1} \rangle$.

Equation (4.15) is one of our main new analytic results. The first term is a modification of the standard Peebles recombination rate with $C \to C^{\rm mix}$. The second term, proportional to $1 - C^{\rm mix}$, is a qualitatively new term, which accounts for the spatial mixing of Lyman-α photons. This term could in principle have a *very* significant effect on the net recombination rate when $C^{\rm mix} \ll 1$. However, it averages to zero, hence should produce a relatively minor effect on the average free-electron density, as we will indeed confirm below.

4.3 Illustration with simple 2-zone model

To illustrate the difference between the no-mixing and full-mixing regimes, we consider a toy model in which the Universe consists of equi-probable regions with baryon overdensities $\Delta^\pm = \rho_b^\pm / \langle \rho_b \rangle = n_{\rm H}^\pm / \langle n_{\rm H} \rangle = 1 \pm \sqrt{b}$, where b is the baryon clumping parameter, which we shall take to be constant $b = 0.5$.

In each case, we solve for the free-electron fraction $x_e \equiv n_e/n_{\rm H}$ in each zone, and then compute the "global" free-electron fraction X_e, through

$$X_e \equiv \frac{\langle n_e \rangle}{\langle n_{\rm H} \rangle} = \frac{1}{2} \left[\Delta^+ x_e^+ + \Delta^- x_e^- \right]. \tag{4.16}$$

In the no-mixing limit, we simply solve two independent ODEs for the ionization fraction $x_e^\pm$ in each "zone". In contrast, in the full-mixing limit, the 2 ODEs are coupled, since they each depend on average quantities such as $\langle n_{1s} \rangle = \langle n_{\rm H} \rangle (1 - X_e)$.

We show the solutions in the two limit cases in figure 6. The left panel shows the separate evolutions of $x_e^\pm$ in the no-mixing and full-mixing limits, and the right panel shows the evolution of the global ionization fraction X_e in both limits. We see that, first of all, the deviation of X_e from the standard ionization fraction is typically much smaller than the deviations of the ionization fractions in each zones. Second, we see that the evolution of X_e in the no-mixing and full-mixing limits are very similar. We will however see that there are more significant deviations between these two limits in the realistic case of a Batchelor spectrum (section 5), particularly at lower redshifts.

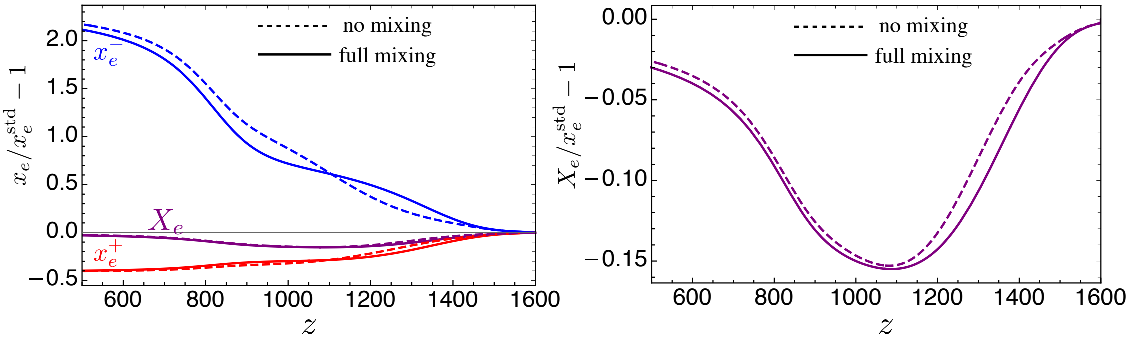

Figure 6. Change in the free-electron fraction relative to the standard history, in a simple toy model with two equi-probable zones with baryon densities $\rho_b^{\pm} = \langle\rho_b\rangle(1 \pm \sqrt{b})$, with clumping parameter $b = 0.5$, in the no-mixing limit (dashed), and in the full-mixing limit (solid). *Left*: separate evolution of x_e^+ (red), x_e^- (blue) and $X_e \equiv \langle n_e\rangle/\langle n_{\rm H}\rangle$ (purple). *Right*: zoom-in on the evolution of X_e in the no-mixing and full-mixing limits. We see that the two limits give very similar results.

5 A realistc calculation of recombination in the presence of primordial magnetic fields

In this section we show results for the typical perturbations in the ionization fraction during recombination in a magnetized Universe. We first present some general results and then consider the best strategy to obtain precise results. All calculations in this section assume non-helical PMFs with a Batchelor spectrum and if not otherwise stated, are performed in the limit of full mixing, i.e. using eq. (4.15) for the net recombination rate.

5.1 General trends

PMF evolution in the early Universe is described by freely decaying MHD. Individual magnetic modes excite fluid motions which then dissipate. Before recombination those fluid motions are associated with baryon clumping which then decays again. As a first application of our code we determine when a particular magnetic mode of given proper scale L and field strength B is dissipated. We define this time approximately by the time of maximum clumping. In [25] an analytic model based on numerical results was developed. It found that magnetic modes dissipate when the eddy turn-over time approximately equals the Hubble time, i.e. when $L \approx {\rm v}/H$, where v are the peculiar motions excited by the magnetic field. During recombination the fluid undergoes a transition from viscous MHD, when the photon drag coefficient α defined in eq. (2.5) is much greater than the expansion rate H, to turbulent MHD when α falls below H due to the drop in electron density.

In the viscous regime $\alpha \gg H$ peculiar velocities may be estimated by ${\rm v} \approx {\rm v}_{\rm A}^2/(\alpha L)$, implying ${\rm v} \approx {\rm v}_{\rm A}/\sqrt{\alpha/H}$, whereas in the turbulent regime, ${\rm v} \approx {\rm v}_{\rm A}$. We can combine the two regimes by approximating ${\rm v} \approx {\rm v}_{\rm A}/\sqrt{1+\alpha/H}$, implying the following expression for L

$$L \approx \frac{{\rm v}_{\rm A}}{\sqrt{H(\alpha+H)}}\,, \tag{5.1}$$

giving the length scale which is dissipated as a function of redshift and magnetic field strength. In figure 7 the dotted lines show the prediction for two different field strengths. This can be compared to the results of the code when magnetic plane waves of wavelength L are

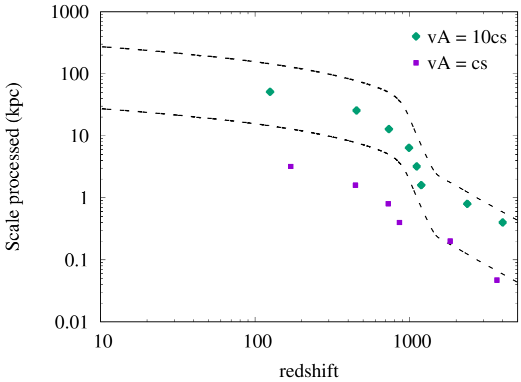

Figure 7. Comparison of numerically obtained and theoretically inferred redshifts $z_{\rm diss}$ of the dissipation of magnetic modes as a function of their comoving scale, for two different field strength, i.e. $\mathrm{v}_A = 1$ and $10c_s$ before recombination. The theoretical prediction (see text) is given by the dotted lines, whereas the numerically determined redshifts are shown by the green ($\mathrm{v}_a = 10c_s$) and purple ($\mathrm{v}_a = c_s$) points. The numerical "experiments" evolve one magnetic mode of a fixed comoving scale and the redshift of dissipation is defined as the redshift of maximum clumping.

evolved from early times (the green and purple points). It is observed that the theoretical approximation is good at early times $z > 1000$ but deviates from the numerical results at lower redshift (or larger scales). Figure 7 is therefore useful to find those magnetic modes which induce the maximum clumping shortly before recombination. The clumping induced by modes smaller/larger that this mode is already decaying/has not fully developed yet.

Next we consider the impact of individual effects on the ionization fraction X_e and the evolution of the clumping factor. We use the same PMF spectrum as that with results shown in figures 1 and 2, but omit particular effects. In figure 8 we show results for the perturbation in the ionization fraction. The purple line shows results when the reduction of speed of sound during recombination is taken into account and full Lyman-α photon mixing between different regions is assumed. The orange line shows results when instead of full mixing $f_\alpha = 1$, mixing according to the Monte-Carlo simulations in section 4 (i.e. figures 4 with mixing "length" 3 kpc) is assumed. It is seen that the deviations between the two is very small. The blue line shows results for full mixing but not taking into account of the reduction of speed of sound during recombination. Here a deviation of order 10 per cent is observed. Somewhat larger deviations are attained when Lyman-α photon mixing is neglected shown by the green line. Coincidentally, in this case X_e is close to that of the three-zone model M1 with $b = 0.5$.

In the right panel of figure 8 we show the evolution of the clumping factor with the same different physical effects considered in the left panel. The reduction of speed of sound enhances clumping, whereas as expected, details of Lyman-α transport do not have an effect on clumping. It is noted that in all cases, the final field at redshift $z = 10$ is 4.38×10^{-2} nG. Some residual clumping of $b \approx 0.1$ survives to low redshifts.

The MHD simulations of the PMF evolution assume as initial condition a particular random realization of the spectrum. It is important to know if different random realizations result in deviating X_e predictions, in particular, if there is realization variance. We have compared results for three different random realizations of the PMF field. We found that the global ionization fraction X_e varies by at most $\sim 1\%$ between different realizations. Hence

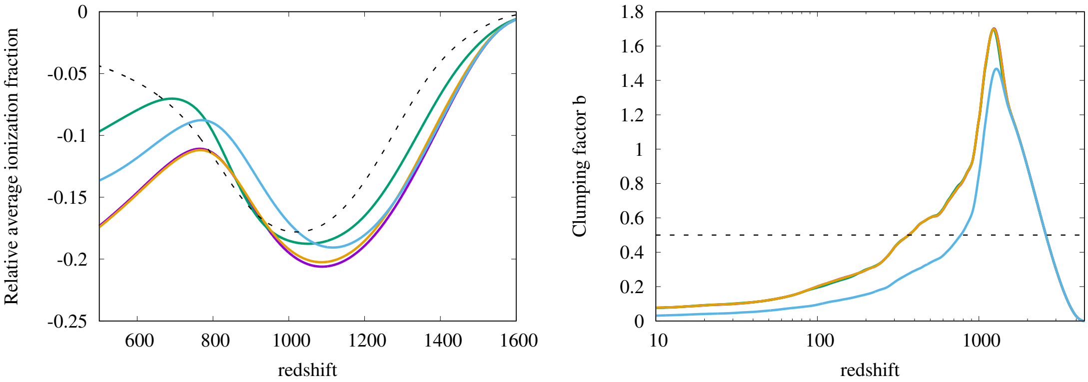

Figure 8. Relative change of the global ionization fraction X_e when compared to a homogeneous Universe without PMFs (*left*) and evolution of the clumping factor (*right*), for a number of 256^3 numerical simulations of a non-helical PMF with Batchelor spectrum. Initial conditions were chosen as $V_{A,\mathrm{rms}} = 12c_s$ and $L_{\mathrm{box}} = 24\,\mathrm{kpc}$ with all modes in the range $3\,\mathrm{kpc} \leq \lambda \leq 24\,\mathrm{kpc}$ excited. In both panels, the different lines correspond to: full Lyman-α mixing, i.e. $f_\alpha = 1$ (purple), no Lyman-α mixing, i.e. $f_\alpha = 0$ (green), Lyman-α mixing as given by the MC results of the last section with mixing length scale 3 kpc (orange), and full Lyman-α mixing but with the reduction of speed of sound during recombination neglected (blue). For comparison, the dotted line shows results of the M1 three-zone model (no Lyman-α mixing) for clumping factor $b = 0.5$. It is seen that the reduction of speed of sound during recombination has a some impact on b, whereas details of the Lyman-α mixing do not.

the realization variance is well below the overall effect of PMFs on X_e, which is of order 20%. We also found that the clumping factor vary by at most $\sim 10\%$, well below peak clumping of order $b \sim 2$. We conclude that realization variance is of order $\sim 5\%$ of the effects we compute, and may be safely neglected.

5.2 Optimizing calculations for non-helical magnetic fields with a Batchelor spectrum

It is our ultimate goal to calculate accurately the changes in ionization fraction ΔX_e as a function of final surviving rms magnetic field B_f strength. Here define B_f as the total surviving root-mean-square magnetic field at redshift $z = 10$. Though in principle our code can accomplish this, in practice we have the limitation of feasible numerical resolution. In particular, there are three mutually possibly conflicting requirements on numerical resolution:

- Each individual Fourier mode has to be resolved sufficiently to obtain convergence of results as a function of resolution. In appendix C we demonstrate that in order to have approximately $\sim 10\%$ accurate results in ΔX_e and B_f, individual modes have to be resolved at least with resolution 32^3, preferably 64^3.
- All magnetic modes which contribute to B_f and whose induced clumping effects ΔX_e have to be included. Referring to figure 7 we see that a larger range of scales is processed before and during recombination, potentially requiring very large numerical resolutions.
- There has to be a larger number of those magnetic modes which mostly influence ΔX_e (those which produce the peak in clumping shortly before recombination) as otherwise there could be large realization variance.

To illustrate the point more clearly. Given a simulation box of physical size $L_{\rm box}$ we can populate randomly all modes $k_i = (2\pi/L_{\rm box})n_i$, where n_i are integers with i denoting spatial direction. If we populate all modes $n = \sqrt{n_1^2 + n_2^2 + n_3^2} \leq 8$, we need at least 256^3 resolution in order to resolve all modes with at least 32^3. If we identify the $n_{\rm rec} \approx 6 \pm 1$ modes with those which have the main impact on recombination there will be not much realization variance, as there are many modes $\sim n_{\rm rec}^2 \Delta n_{\rm rec} \sim 72$. That was the case for all the simulations shown so far (cf. discussion at the end of section 5.1). However, in that case we will not be able to populate ultraviolet modes larger than $k_{\rm max} = (4/3)k_{\rm rec}$. Those ultraviolet modes will still have an influence on recombination due the residual clumping they had produced and due to mode-mode coupling. Vice versa, if we take $k_{\rm max} = 4k_{\rm rec}$ as to include enough UV modes, than there should be significant realization variance as there are only $\sim n_{\rm rec}^2 \Delta n_{\rm rec} \sim 4$ of the most important modes for recombination. We will investigate uncertainties due to missing ultra-violet modes and realization variance further below.

We will now demonstrate that the easiest spectra to simulate are those of phase-transition generated non-helical PMFs with Batchelor spectrum. Considering inflationary fields with approximately scale-invariant spectra we may directly refer to figure 7 to assess the range of scales required to simulate to obtain an accurate result. Taking for example the case $\mathrm{v}_A = 10c_s$, in order to simulate all magnetic modes which dissipate between redshift $z \approx 5000$ and $z \approx 500$, we need to resolve all scales between $L \approx 0.3\,\mathrm{kpc}$ and $30\,\mathrm{kpc}$, implying a dynamic range of ~ 100. This would require simulations with resolution 3200^3 which would require 1000–10000 times larger computer resources than used here.[9] On the other hand, as $B(L) \sim L^{-5/2}$ for Batchelor spectra, the dynamic range required is much compressed compared to scale-invariant fields. Before recombination the mode dissipation redshift $z_{\rm diss}$ scales as $(B/L)^{2/3}$ such that modes a factor two smaller dissipate at a redshift $z_{\rm diss}$ a factor $2^{7/3} \approx 5$ larger. For scale-invariant fields the factor is only $2^{2/3} \approx 1.6$. For fully helical fields with Batchelor spectrum, the necessary dynamic range is also compressed, but not as much as in the non-helical case, as the inverse cascade pushes fields to larger scales.

We will from now on focus on the non-helical Batchelor case. In order to establish which scales need to be resolved in the simulation, we perform a series of smaller simulations. The scales resolved and initial magnetic field strengths $B_{\rm rms}^{\rm ini}$ of these simulations are shown in table 1. Field strength and length scales in all these simulations were chosen as to mimic the Batchelor spectrum, i.e. $B(L) \sim L^{-5/2}$, i.e. Run 1 presents the largest scales with smallest $B_{\rm rms}^{\rm ini}$ and Run 6 presents the smallest scales with largest $B_{\rm rms}^{\rm ini}$. Obtaining results for these simulations allows us, to assess, in the absence of mode-mode coupling, which modes contribute most to the final field strength $B_{\rm rms}^{\rm fin}$ and which modes most to the perturbation in ΔX_e. Results for the evolution of clumping factor, magnetic energy density, and ionization fraction are shown in figure 9. As expected, the peak in the clumping occurs at successively higher redshifts as one goes from Run 1 to Run 6.[10] Run 3 produces the largest clumping right before hydrogen recombination, the "neighboring" runs Run 2 and Run 4 also lead to some significant clumping shortly before hydrogen recombination. This compares well with

---

[9] We note here that 2D simulations significantly overestimate the effects on recombination.

[10] Strictly speaking should Run 5 and Run 6 be started at higher initial redshift. Due to the strength of the photon drag at early times this is however computationally very expansive. We have verified that changing the initial redshift to somewhat higher values does not significantly change the evolution at lower redshift.

Run	Size	$L_{\rm min}$ (kpc)	$L_{\rm max}$ (kpc)	$\mathrm{B}^{\rm ini}_{\rm rms}$ (pG)	$\mathrm{B}^{\rm fin}_{\rm rms}$ (pG)	$z_{\rm diss}$
1	256^3	1.5	6.	21.9	8.54	< 1000
2	64^3	1.03	1.03	51.0	3.54	≈ 1000
3	64^3	0.713	0.713	121	2.77	≈ 1500
4	64^3	0.492	0.492	327	0.865	≈ 3300
5	64^3	0.339	0.339	827	0.627	≈ 7850
6	64^3	0.224	0.224	2093	0.738	≈ 18700

Table 1. Size, minimum scale resolved, maximum scale resolved, initial magnetic field strength, final magnetic field strength, and approximate dissipation redshift estimated from figure 7 for six smaller simulations Run 1–Run 6.

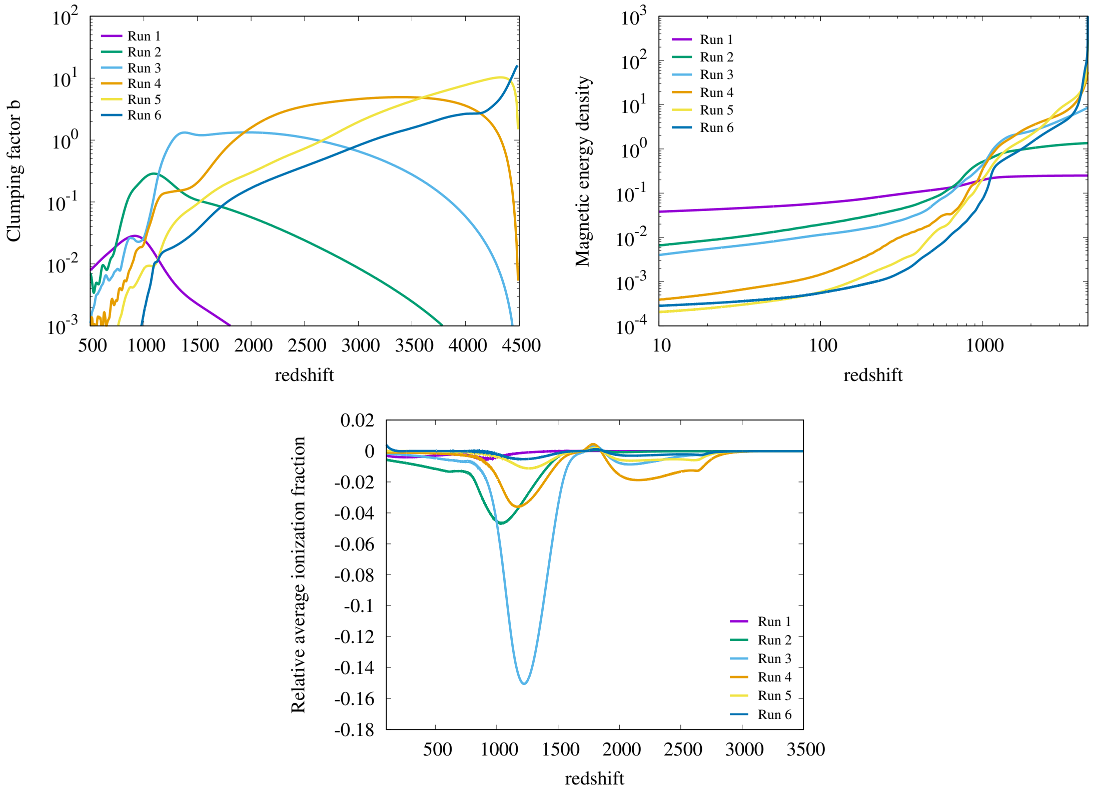

Figure 9. Redshift evolution of the clumping factor (*top*), magnetic energy density (*middle*) and fractional change to the global ionization fraction (*bottom*) for the simulations Run 1–Run 6. Here a value of unity for magnetic energy density corresponds to a field strength of $\tilde{B}_{\rm rms} = 4.38 \times 10^{-2}\,$nG.

the analytic estimate of “dissipation” redshift also given in table 1, defined as the redshift of peak clumping for a mode. These are between $z_{\rm diss} \approx 1000$ and 3300 for runs Run 2–Run 4. In the bottom panel of figure 9 we see that indeed X_e is mostly affected by Run 3, and to a lesser degree by Run 2 and Run 4. In the absence of mode-mode coupling effects, one could imagine that only resolving the scales resolved in Run 2 to Run 4, would already lead to a fairly accurate estimate for ΔX_e. This corresponds to a required dynamic range of only two.

Run	Size	$L_{\rm min}$ (kpc)	$L_{\rm max}$ (kpc)	$\rm B_{rms}^{ini}$ (pG)
7	256^3	1.	8.	60.4
8	256^3	0.339	1.5	900
9	256^3	0.234	1.5	2278
10	256^3	0.1875	1.5	3966

Table 2. Size, minimum scale resolved, maximum scale resolved, and initial magnetic field strength for Run 7–Run 10.

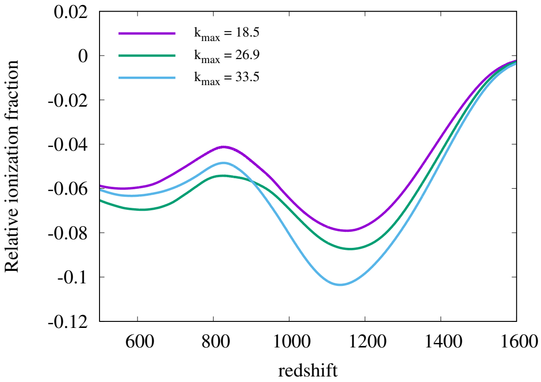

Figure 10. Dependency of ΔX_e on the ultraviolet cut-off of the magnetic field spectrum. Each curve represents the average ΔX_e of four different random realizations of a PMF with Batchelor spectrum. It is seen that including higher-k modes, which dissipate well before recombination (i.e. at $z_{\rm diss} \approx 2 \times 10^4$ for Run 9 and $z_{\rm diss} \approx 3.3 \times 10^4$ for Run 10) do have impact on ΔX_e due to mode-mode coupling.

Inspecting the middle panel of figure 9 one infers that the final magnetic field is dominated by the larger modes resolved in Run 1 with a subdominant contribution from Run 2 and Run 3.

This suggests the following strategy to obtain relatively precise results. The final magnetic field strength may be obtained by a simulation of the relevant larger scales, whereas ΔX_e may be obtained by an independent simulation of the relevant smaller scales. In table 2 we show the size, resolved scales, and initial magnetic field for simulations to obtain the final field (Run 7) and the impact on X_e (Run 8–Run 10). Here Run 8 resolves all scales of Run 2–Run 5. In figure 10 we show averaged results of three realizations of each Run 8–Run 10. It is seen that including even smaller modes than initially deemed necessary from the results of Run 2–Run 6 have impact on ΔX_e. There is a significant difference in ΔX_e between Run 8 and Run 9, which becomes even larger between Run 8 and Run 10. The smallest modes in Run 10 have $z_{\rm diss} \approx 3.3 \times 10^4$ and due to mode-mode coupling effects still have an important effect on X_e. Such small modes naively thought to dissipate at high redshift should therefore still be included. We are currently not able to assess if the inclusion of even smaller modes further enhances the X_e reduction. We note here that a 256^3 simulations requires already significant computing power, i.e. approximately 2 CPU-years. This is mostly due the exceedingly small drag time $1/\alpha$ at higher redshifts.

As it is necessary to include more UV modes, the $n_{\rm rec}$ for Run 10 is only two. We therefore expect significant realization variance. In figure 11 the average ΔX_e is shown for

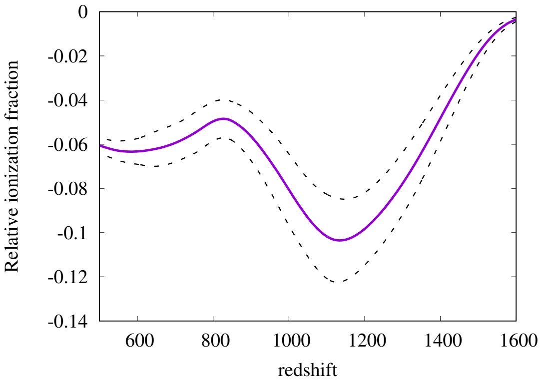

Figure 11. The average ΔX_e and one-sigma ranges of three different random realizations of a PMF with Batchelor spectrum Run 10. It is seen that random realization uncertainties are substantial, around $\sim 20\%$. This is in contrast do the small realization variance found for the results displayed in figure 8, since those simulations included a large number of modes dissipating during recombination, but did hardly include important ultra-violet modes.

Run 10, albeit based only on four different realizations. The dotted lines show the average plus, minus one standard deviation. It is observed that realization variance is significant, $\sim 20\%$, such that it is preferable to reduce the error due to realization variance by averaging the result of a larger number of simulations with different realizations.

6 The combined effects of plasma heating and baryon clumping

It is well known [61] that the decay of magnetic turbulence induces a heat source for the baryons which may influence the ionization fraction X_e substantially at lower redhifts. Similar holds for ambipolar diffusion at even lower redshifts. An increase of the baryon temperature T_b over that of the CMB T_{CMB} lowers the temperature-dependant recombination rate which leads to higher residual ionization fractions. The evolution of the baryon temperature with time t is given by (2.8). At redshifts $z \approx 1000$ the ionization fraction is still fairly high $X_e \approx 0.1$ such that baryon cooling by electron Thomson scattering on CMB photons keeps T_b very close to T_{CMB}. However, at slightly lower redshifts $z \approx 900$ when $X_e \approx 10^{-2}$ the heating of baryons due to the dissipation of magnetic fields can significantly increase the baryon temperature. This in turn reduced the temperature dependent recombination rate which leads to higher residual X_e.

A higher residual X_e in the redshift range $\sim$ 400–900 induces a suppression of the CMB anisotropies at higher multipoles due to residual scatterings of photons out of the beam. It also introduces a feature at small multipoles $l \sim$ 100–200. These effects may be constrained by high-precision CMB data, as has been done in [57, 62, 64, 120, 121]. These authors used an analytic expression from [61] to approximate the heating rate due to magnetic field dissipation. The only study which attemps to compute the heating rate numerically [122] could not simulate at higher magnetic field strength, as they were facing the complication of baryon clumping, which many MHD solvers have problems with. We introduced heating of baryons due to magnetic field dissipation in the modified ENZO code. To this end we

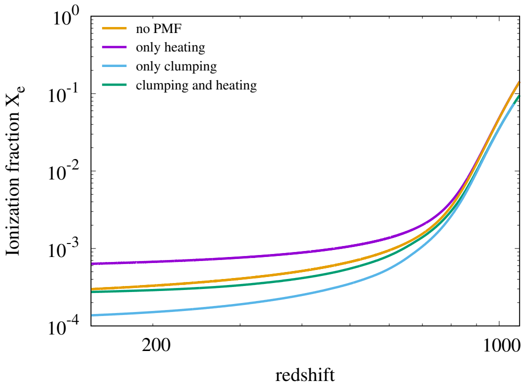

Figure 12. The ionization fraction X_e as a function of redshift for four different cases: the homogeneous case without clumping and dissipation (orange), the inhomogeneous case due to baryon clumping, but without dissipation (blue), the homogeneous case without clumping but with dissipation (purple), and the realistic inhomogeneous case with clumping and dissipation (green).

use a uniform heating rate[11]

$$\Gamma = \frac{1}{\mathrm{V}} \frac{d}{dt} \int d\mathrm{V} \left(\frac{1}{2} \rho_b \mathbf{v}^2 + \frac{1}{8\pi} \mathbf{B}^2 \right) , \tag{6.1}$$

which allows us to evolve the local baryon temperature. We did not consider the less important heating due to ambipolar diffusion. We are thus able, for the first time, to treat both effects, clumping and heating at the same time.

Results are shown in figure 12. Here a particularly strong magnetic field with Batchelor spectrum was chosen, with remaining magnetic field strength of 1.2 nG at $z = 1088$ leading to a final field of 0.13 nG at redshift $z = 10$. According to [121], which give the limit $B < 0.18$ nG at $z = 1088$ such a field should be clearly ruled out due to heating. It should also be ruled out due to clumping, if the three-zone model M1 with older data is used [88], due to modifications of X_e at $z \approx 1100$ rather than at $z \approx 400$–900. In figure 12 one sees the ionization fraction for four different simulations. The orange line shows X_e for a homogeneous Universe with no magnetic fields. The purple line shows X_e when the heating rate is extracted from the MHD simulation and used in a homogeneous Universe. This corresponds to the evolution of X_e computed in [121] with the difference that the heating rate is not taken from an analytic approximation but computed directly in the code. This case seems clearly ruled out by current CMB data. The blue line shows X_e when heating is not taken into account, but the baryon inhomogeneities, i.e. clumping, are. In this case the average X_e is lower than in the no magnetic field case, and taking only the low z evolution into account the model should not be ruled out. The same holds for the realistic case, when clumping and heating is taken into account, which is shown by the green line. The realistic case in fact is very close to the no magnetic field case at low redshifts. Baryon heating due to magnetic field

---

[11] Magnetic- and kinetic- energy dissipation here occurs over numerical viscosity, which is a common practice in MHD simulations in astrophysics [123]. In principle we could have computed the local dissipation rate when using the standard energy evolution equation in *ENZO* amended by CMB cooling/heating, as *ENZO* conserves energy. However, we do not think that the approximation of applying a global average homogeneous heating rate could change our conclusions below drastically.

dissipation increases X_e at lower redshift, whereas the clumping of baryons decreases X_e with the net effect being only small change from the no magnetic field case. In fact we have performed many more simulations with varying magnetic field strengths including the effects of clumping and heating and in none of these simulations have we ever found an increased X_e. We conclude therefore, that current limits on PMFs from baryon heating do not apply, as they have not taken into account clumping. We stress, that constraints on this model come from clumping, and the associated changes of X_e around the peak of the visibility function at $z \approx 1090$, inducing a change in the sound horizon, modified Silk damping, and a change in the width of the visibility function, but not from hydrodynamic heating.

7 Conclusions

In this paper we presented an in depth analysis of the effects of primordial magnetic fields on the process of cosmic recombination. It had been shown priorly that PMFs of sufficient magnitude lead to non-linear inhomogeneities in the baryons (clumping) on small scales before recombination, and that this clumping could result in a partial solution to the cosmic Hubble tension. However, prior analysis was in large parts based on approximative three zone models and omitted a number of physical effects. For our analysis we employed full 3D MHD simulations including the effects of photon drag and cosmic expansion. These MHD simulations were coupled to a new recombination code, sufficiently accurate to obtain $\sim$ 10–20% accurate results in the relative perturbation of the ionization fraction $\Delta X_e/X_e$ due to the existence of PMFs. We employed detailed Monte-Carlo (MC) simulations of Lyman-α photon propagation in space and frequency. These simulations establish that for the typical peculiar flows found in the MHD simulations for observationally allowed PMF strengths, the Lyman-α photon escape fraction due to redshifting is not much changed from that in an unmagnetized Universe. However, the MC simulations also established that Lyman-α photons are almost fully mixed between underdense- and overdense- regions such that the recombination process is no further local. We derived an analytic result for the recombination process in an inhomogeneous Universe with fully mixed Lyman-alpha photons, which leads to a reduction of the average ionization fraction compared to the non-mixed case. We investigated the dependence of results for PMFs with Batchelor spectrum on ultra-violet magnetic modes and found some unexpected dependency.

Our study may serve as the theoretical foundation of a precise comparison between the theory of recombination with PMFs and CMB observations.

Acknowledgments

We acknowledge Levon Pogosian for a multitude of useful conversations and much emotional support to conclude this lengthy project. We also acknowledge many useful exchanges with Jens Chluba, as well as Andrey Saveliev. This research was enabled in part by support provided by WestGrid (https://www.westgrid.ca) and the Digital Research Alliance of Canada (https://alliancecan.ca). This work was partially supported by the U.S. Departement of Energy SLAC Contract No. DE-AC02-76SF00515. YAH is a CIFAR-Azrieli Global Scholar and acknowledges support from the Canadian Institute for Advanced Research (CIFAR), and is grateful to be hosted by the USC departement of physics and astronomy while on sabbatical.

A Monte Carlo simulations of the Lyman-α escape fraction

The thermally averaged cross section[12] for a Lyman-α photon to scatter of a hydrogen atom in the $1s$ ground state is given by

$$\langle\sigma\rangle_{\rm th} = \frac{1}{(2\pi)^3}\int {\rm d}\Omega\,{\rm d}p\,p^2\left(\frac{2\pi}{mT}\right)^{3/2}\exp\left(\frac{-p^2}{2mT}\right)\sigma(\mathbf{p})\,, \tag{A.1}$$

where m is hydrogen mass. Here the cross section is given by

$$\sigma = \frac{3\lambda_\alpha^2}{8\pi}\,\frac{\Gamma_\alpha^2}{(\omega_r-\omega_\alpha)^2+\Gamma_\alpha^2/4}\,, \tag{A.2}$$

where ω_r and ω_α are photon circular frequency in the atomic rest frame and the Lyman-α circular frequency, respectively, λ_α is the Lyman-α wavelength, and Γ_α is the decay rate of the excited $2p$ state back to the ground state. Here ω_r relates to the photon frequency ω in the gas rest frame

$$\omega_r = \omega\left(1-\frac{p_\parallel}{m}-U_\parallel\right), \tag{A.3}$$

where $p_\parallel = \hat{\mathbf{k}}\cdot\mathbf{p}$ and $U_\parallel = \hat{\mathbf{k}}\cdot\mathbf{U}$ are the atomic momentum and fluid velocity parallel to the photon direction given by the unit vector $\hat{\mathbf{k}}$. Introducing the new variable

$$x = \frac{(\omega-\omega_\alpha)}{\omega_\alpha {\rm v}_{\rm th}} \tag{A.4}$$

where ${\rm v}_{\rm th} = \sqrt{2T/m}$ as well as $\tilde{p} = p/\sqrt{2mT}$ one can rewrite the thermally averaged cross section as follows

$$\begin{aligned}\langle\sigma\rangle \;=& \left(\frac{1}{\sqrt{\pi}}\int {\rm d}\tilde{p}_{\perp 1}\exp(-\tilde{p}_{\perp 1}^2)\right)\left(\frac{1}{\sqrt{\pi}}\int {\rm d}\tilde{p}_{\perp 2}\exp(-\tilde{p}_{\perp 2}^2)\right)\\ &\cdot\left(\frac{1}{\sqrt{\pi}}\int {\rm d}\tilde{p}_\parallel\,\frac{\exp(-\tilde{p}_\parallel^2)\sigma_0\Gamma_\alpha^2}{\omega_\alpha^2 v_{\rm th}^2(x-\tilde{p}_\parallel-U_\parallel/v_{\rm th})^2+\Gamma_\alpha^2/4}\right)\end{aligned} \tag{A.5}$$

where $\sigma_0 = 3\lambda_\alpha^2/8\pi$. Eq. (A.5) has been written as an equation immediately usable for Monte Carlo methods. First note that the first two terms in brackets are unity. The third term in brackets is thus simply $\langle\sigma\rangle$. In the Monte Carlo we try to sample one-dimensional cumulative distributions between zero and unity by randomly generated numbers between zero and unity. Eq. (A.5) can be used for that to obtain the likely hydrogen $(\tilde{p}_{\perp 1},\tilde{p}_{\perp 2},\tilde{p}_\parallel)$ on which the photon scatters. Given those, one may compute the new frequency of the photon after scattering. After performing three successive Lorentz transformations, first from the gas rest frame at emission to the gas rest frame at absorption, than from the gas rest frame at absorption to the atomic rest frame, and than vice versa, and assuming that ${\rm v}_{\rm th}, U \ll 1$ and that atomic recoil can be neglected, we find

$$x_{\rm out} \approx x_{\rm in} - \frac{(U_\parallel^{\rm abs}-U_\parallel^{\rm em})}{v_{\rm th}} - \tilde{p}_\parallel(1-\mu) + \tilde{p}_\perp\sqrt{1-\mu^2}\cos(\beta)\,, \tag{A.6}$$

---

[12] Note that in this section all units are natural, i.e. $\hbar = c = k = 1$. In case numerical values are given they refer to values at redshift $z = 1100$, close to the standard recombination redshift.

Here the rescaled photon frequencies $x_{\rm in}$ and $x_{\rm out}$ refer to the frequency in the gas rest frame at the location of emission and the frequency after re-scattering in the gas rest frame at the location of absorption, whereas $U_{\|}^{\rm abs}$ and $U_{\|}^{\rm em}$ are the fluid velocities parallel to the photon momentum at the location of absorption and emission, respectively. Furthermore, $\tilde{p}_{\perp} = \sqrt{\tilde{p}_{\perp 1}^2 + \tilde{p}_{\perp 2}^2}$ is the total perpendicular rescaled momentum, $\mu = \hat{k}_{\rm in} \cdot \hat{k}_{\rm out}$ is the cosine of the scattering angle between the incoming and outgoing photons, and β is another scattering angle between zero and 2π. We note that beta always has a flat distribution and μ is flat in the interval $[-1, 1]$ for isotropic scattering, but not for dipole scattering.

After absorption of a line photon the hydrogen atom is in a metastable $2p$ state. In most cases it will spontaneously de-excite into the $1s$ state by re-emission of a Lyman-α photon with frequency $x_{\rm out}$. However, on rare occasions $\sim 10^{-7}$ the metastable $2p$ state will be photo-ionised by CMBR photons or decay via the two-photon transition.[13] It is evident that the small probability for reionsation makes a Monte-Carlo very challenging, as a larger number of interactions have to be followed before the fate of the Lyman-α photon is known.

Our Monte-Carlo simulation proceeds as follows

(1) Inject a photon with frequency $x = 0$ at a random location (we checked explicitly that injecting it from a Voigt profile does not change results)

(2) Compute the thermally averaged cross section σ and the photon mean free path $l_\gamma = 1/(\sigma n_{\rm H})$ where $n_{\rm H}$ is the neutral hydrogen density

(3) Advance the photon over a path length $Dl = \epsilon l_\gamma$. Here values of $\epsilon = 10^{-1}$–10^{-2} are used and results are independent of it.

(4) Redshift the photon by an amount $\Delta x = -HDl/{\rm v}_{\rm th}$

(5) Determine probalistically if the photon scatters after having traveled distance Dl. This is the case when a random number between zero and unity is larger that $\exp(-\epsilon)$.

(6) If not return to (2), if yes proceed to (7)

(7) Determine via random number if (a) a Lyman-α photon is re-emitted (i.e. re-scattering of the Lyman-α photon or the much less likely alternatives (b) the intermediate $n = 2$ state is reionised or (c) the state decays via a two-photon transition. In case (a) go to (8), in case (b) and (c) proceed to the next injected photon (1) where in (b) no net recombination has occurred, and in (c) it has.

(8) Using three random numbers determine via eq. (A.5) the probable $\tilde{p}_{\|}$, $\tilde{p}_{\perp 1}$, and $\tilde{p}_{\perp 2}$ of the scattering atom. Using two more random numbers determine μ and β and compute the new gas rest frame frequency $x_{\rm out}$ from eq. (A.6). Return to (2).

Lyman-α photons which are lost since they redshifted out on the red wing out of resonance may be identified as the loop does not leave anymore the range (2)–(6). These

---

[13] On less rare occasions $\sim 10^{-4}$ the hydrogen atom will be further excited by CMBR photons into $n > 2$ levels. These higher excitations will with near unity probability eventually de-xcite into the ground state with the generation a new Lyman-α photon. We do not treat this process in the current Monte-Carlo.

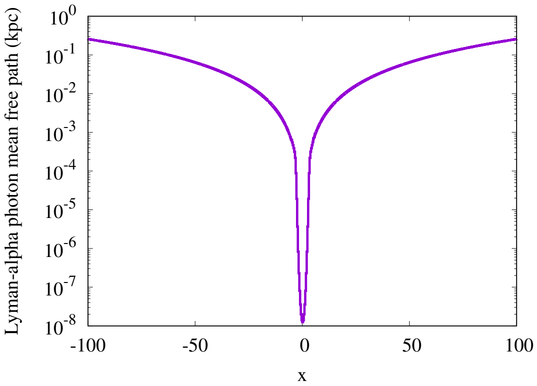

Figure 13. Comoving Lyman-α photon mean free path in as a function of photon frequency x at redshift $z \approx 1100$.

photons never reach (7), thus never scatter anymore, and their frequency becomes ever smaller. Accounting for the numbers of different scenarios it is straightforward to compute the well-known Peebles factor C eq. (3.9).

The mean free path as a function of frequency is shown in figure 13. It is seen that it is extremely small (e.g. compare for example to the horizon $l_{\mathrm{H}} \sim 100\,\mathrm{Mpc}$. Taking into account that $\sigma \sim 1/x^2$ on the wing, even photons on the extreme thermal red wing, i.e. $x \sim -10^5$ may still scatter. However, at such small x between each scattering the frequency redshifts further, reducing the cross section even more, such that the photons with exceedingly high probability become inert (except if reionisation happens during those few last scatterings). One may estimate the x at which the probability for the Lyman-α photon becoming inert for the $1s$-$2s$ transition is approximately fifty percent. One can show [124] that on the wing the probability distribution function $P(x_{\mathrm{out}})$ one obtains from eq. (A.6) is approximately given by a Gaussian with width unity and centered on $x_{\mathrm{out}} = x_{\mathrm{in}} - 1/x_{\mathrm{in}}$. That is x performs a random walk during the many scatterings with, however, a drift term which pulls it back to the center of the line $x = 0$. This drift term competes with the drift away from the center of the line due to redshifting. Demanding approximate equality between these two drift terms

$$-\frac{H}{\sigma(x_{50})n_{\mathrm{H}}\mathrm{v}_{\mathrm{th}}} \approx \frac{-1}{x_{50}} \tag{A.7}$$

one obtains at which x_{50} the probability is approximately 50% to loose the photon. We obtain $x_{50} \approx 60$ which is confirmed by the simulations. At this frequency the mean free path is approximately comoving $0.1\,\mathrm{kpc}$ and as the frequency hovers often for many scatterings around x_{50} the distance traveled is easily in the larger than kpc regime, the scale on which magnetic fields excite inhomogeneities in density and flow.

We present next how the results of our Monte-Carlo simulation in a homogeneous Universe compares to the theoretical C-factor. We consider this as our test problem for the routine of these somewhat challenging simulations (the evolution of one photon takes on average ~ 20 seconds). Figure 14 shows the MC results compared to eq. (3.9) for varying Hubble constants, setting $\Lambda_{2\gamma}$ to zero.[14] It is seen that the comparison is close to perfect. This

---

[14] Our simulations reproduce well photon loss due to the $2s$-$1s$ two γ transition.

JCAP03(2025)012

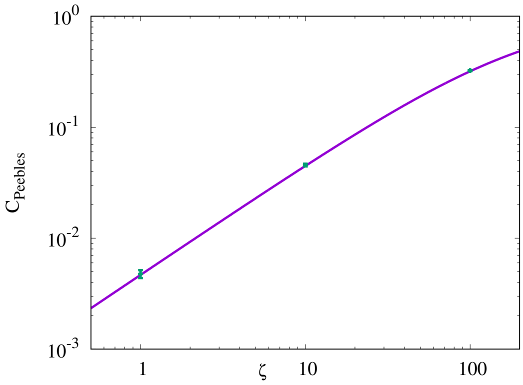

Figure 14. Comparison of the theoretical and Monte-Carlo derived value of the C factor eq. (3.9) in a homogeneous Universe, employing $\Lambda_{2\gamma} = 0$, as a function of ζ, where the cosmological expansion is given by ζH. Here H is the correct Hubble rate at recombination. The solid line shows the theoretical value whereas the points with error bars show results of the MC simulation.

and the test displayed in figure 5 for Lyman-α escape in the presence of bulk flows gives us confidence that our Monte-Carlo simulation is reliable.

B Helium recombination

The details of helium recombination are not crucial for the purposes of this work: the first helium recombination takes place around $z \sim 6000$, before the beginning of our simulations, and during the second helium recombination the free-electron fraction is limited to the range $1 \leq x_e \leq 1.08$, regardless of the details of the recombination process. Changes to the ionization history during helium recombination are also less critical to CMB anisotropies. We therefore defer a detailed study to future work, and in the meantime have implemented a simple 3-level model for helium, accounting only for transitions from the singlet $2P$ state (the equivalent of the hydrogen Lyman-α line), and for hydrogen continuum opacity, but neglecting transitions from the triplet $2P$ state. We adopt the simple model of ref. [109]. We also ran an MC simulation for the Lyman-α transition in Helium and found an even larger mixing fraction (i.e. smaller propagation distances) than for hydrogen, so that Helium recombination can also be assumed to proceed in the “full-mixing” regime. We implemented the full-mixing regime in a similar fashion as for hydrogen.

C Convergence study

In this appendix we briefly study the convergence of results with the number of employed zones. Figure 15 shows the evolution of clumping factor, magnetic energy density, and ionization fraction X_e for a particular PMF spectrum and amplitude for three different resolutions, 64^3, 128^3, and 256^3. As modes only up to $k = 2$ are excited, these modes are effectively resolved by 32, 64, and 128 zones, respectively. From figure 15 it is seen that convergence in the clumping factor is not attained. In particular, the higher the resolution, the higher the clumping factor. This is because the clumping factor is dominated by the very few highest density regions, which can only be resolved with a large number of zones. On

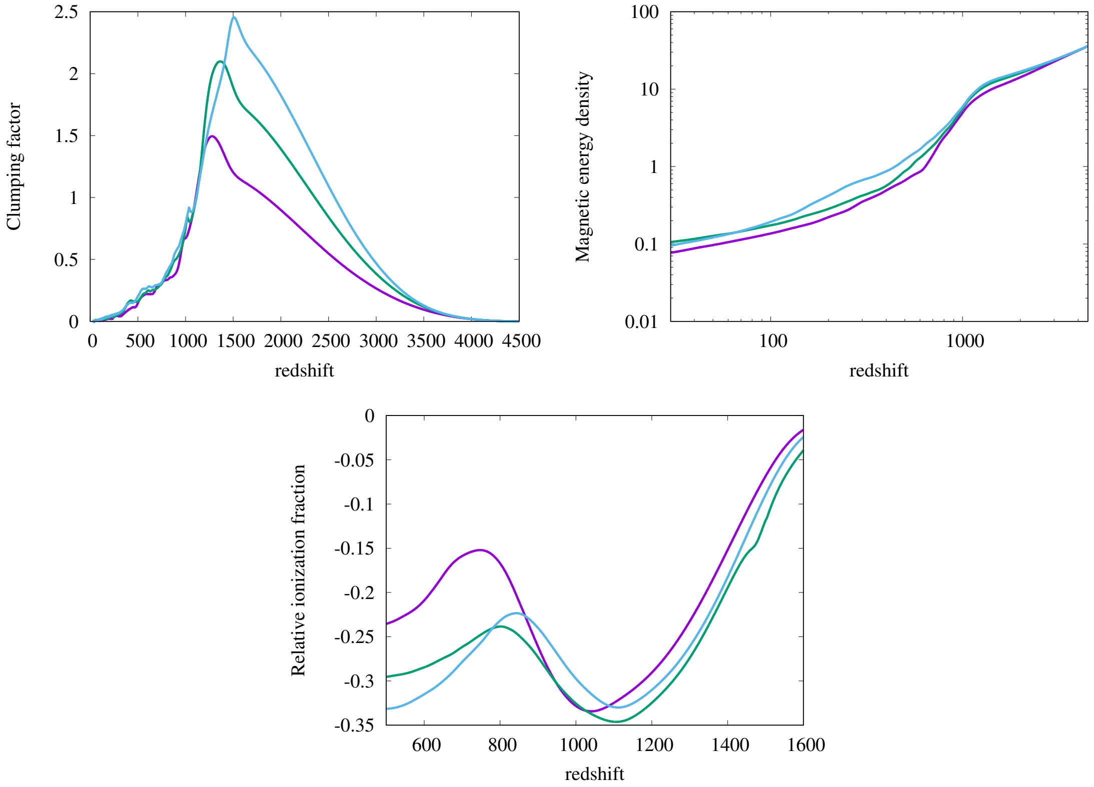

Figure 15. Evolution of the clumping factor b (*top*), magnetic energy density (*middle*) and change to the global free-electron fraction (*bottom*) for different resolutions of the simulation. The simulation box is 6kpc and $\mathrm{v}_A^{\mathrm{rms}} = 30c_S$. All modes with $k \leq 2$ have been randomly excited. Here a mode is given by $\mathrm{v}_A(x) = \mathrm{v}_A^k \sin(2\pi kx + \phi_k)$ in a simulation box $0 \leq x \leq 1$ and v_A^k and ϕ_k are random amplitude and phase for the mode k. A non-helical magnetic field with a Batchelor spectrum has been assumed. The pink, green, and blue lines are for resolutions 64^3, 128^3, and 256^3, respectively.

the other hand, figure 15 shows that approximate convergence in magnetic energy density and X_e is attained even at lower resolution. This is possible because those very high-density regions, which are not properly resolved, recombine very early independently of the exact overdensity. As they are rare as well, no significant impact on X_e is observed. We infer that 32 or 64 zones per Fourier mode should give somewhat accurate results.

References

[1] K. Subramanian, *The origin, evolution and signatures of primordial magnetic fields*, *Rept. Prog. Phys.* **79** (2016) 076901 [`arXiv:1504.02311`] [INSPIRE].

[2] A. Brandenburg and K. Subramanian, *Astrophysical magnetic fields and nonlinear dynamo theory*, *Phys. Rep.* **417** (2005) 1 [`astro-ph/0405052`] [INSPIRE].

[3] R.M. Athreya, V.K. Kapahi, P.J. McCarthy and W. van Breugel, *Large rotation measures in radio galaxies at* $Z > 2$, *Astron. Astrophys.* **329** (1998) 809.

[4] A.M. Wolfe, R.A. Jorgenson, T. Robishaw, C. Heiles and J.X. Prochaska, *An* 84 *microGauss Magnetic Field in a Galaxy at Redshift* $z = 0.692$, *Nature* **455** (2008) 638 [`arXiv:0811.2408`] [INSPIRE].

[5] A. Aramburo-Garcia, K. Bondarenko, A. Boyarsky, A. Neronov, A. Scaife and A. Sokolenko, *The contribution of magnetized galactic outflows to extragalactic Faraday rotation*, *Mon. Not. Roy. Astron. Soc.* **519** (2023) 4030 [arXiv:2204.06475] [INSPIRE].

[6] F. Govoni et al., *A radio ridge connecting two galaxy clusters in a filament of the cosmic web*, *Science* **364** (2019) 981 [arXiv:1906.07584].

[7] T. Vernstrom et al., *Discovery of magnetic fields along stacked cosmic filaments as revealed by radio and X-ray emission*, *Mon. Not. Roy. Astron. Soc.* **505** (2021) 4178 [arXiv:2101.09331] [INSPIRE].

[8] E. Carretti et al., *Magnetic field strength in cosmic web filaments*, *Mon. Not. Roy. Astron. Soc.* **512** (2022) 945 [arXiv:2202.04607] [INSPIRE].

[9] E. Carretti et al., *Magnetic field evolution in cosmic filaments with LOFAR data*, *Mon. Not. Roy. Astron. Soc.* **518** (2022) 2273 [arXiv:2210.06220] [INSPIRE].

[10] A. Neronov and I. Vovk, *Evidence for strong extragalactic magnetic fields from Fermi observations of TeV blazars*, *Science* **328** (2010) 73 [arXiv:1006.3504] [INSPIRE].

[11] F. Tavecchio, G. Ghisellini, L. Foschini, G. Bonnoli, G. Ghirlanda and P. Coppi, *The intergalactic magnetic field constrained by Fermi/LAT observations of the TeV blazar 1ES 0229+200*, *Mon. Not. Roy. Astron. Soc.* **406** (2010) L70 [arXiv:1004.1329] [INSPIRE].

[12] F. Tavecchio, G. Ghisellini, G. Bonnoli and L. Foschini, *Extreme TeV blazars and the intergalactic magnetic field*, *Mon. Not. Roy. Astron. Soc.* **414** (2011) 3566 [arXiv:1009.1048] [INSPIRE].

[13] A.M. Taylor, I. Vovk and A. Neronov, *Extragalactic magnetic fields constraints from simultaneous GeV-TeV observations of blazars*, *Astron. Astrophys.* **529** (2011) A144 [arXiv:1101.0932] [INSPIRE].

[14] I. Vovk, A.M. Taylor, D. Semikoz and A. Neronov, *Fermi/LAT observations of 1ES 0229+200: implications for extragalactic magnetic fields and background light*, *Astrophys. J. Lett.* **747** (2012) L14 [arXiv:1112.2534] [INSPIRE].

[15] K. Dolag, M. Kachelriess, S. Ostapchenko and R. Tomas, *Lower limit on the strength and filling factor of extragalactic magnetic fields*, *Astrophys. J. Lett.* **727** (2011) L4 [arXiv:1009.1782] [INSPIRE].

[16] E.I. Podlesnyi, T.A. Dzhatdoev and V.I. Galkin, *Constraints on the extragalactic magnetic field strength from blazar spectra based on 145 months of Fermi-LAT observations*, *Mon. Not. Roy. Astron. Soc.* **516** (2022) 5379 [arXiv:2204.11110] [INSPIRE].

[17] MAGIC collaboration, *A lower bound on intergalactic magnetic fields from time variability of 1ES 0229+200 from MAGIC and Fermi/LAT observations*, *Astron. Astrophys.* **670** (2023) A145 [arXiv:2210.03321] [INSPIRE].

[18] Z.-Q. Xia, Y. Wang, Q. Yuan and Y.-Z. Fan, *A delayed* 400 *GeV photon from GRB 221009A and implication on the intergalactic magnetic field*, *Nat. Commun.* **15** (2024) 4280 [arXiv:2210.13052] [INSPIRE].

[19] T.A. Dzhatdoev, E.I. Podlesnyi and G.I. Rubtsov, *First constraints on the strength of the extragalactic magnetic field from γ-ray observations of GRB 221009A*, *Mon. Not. Roy. Astron. Soc.* **527** (2023) L95 [arXiv:2306.05347] [INSPIRE].

[20] H.E.S.S. and FERMI-LAT collaborations, *Constraints on the Intergalactic Magnetic Field Using Fermi-LAT and H.E.S.S. Blazar Observations*, *Astrophys. J. Lett.* **950** (2023) L16 [arXiv:2306.05132] [INSPIRE].

[21] Y.-Y. Huang, C.-Y. Dai, H.-M. Zhang, R.-Y. Liu and X.-Y. Wang, *Constraints on the Intergalactic Magnetic Field Strength from γ-Ray Observations of GRB 221009A*, *Astrophys. J. Lett.* **955** (2023) L10 [`arXiv:2306.05970`] [INSPIRE].

[22] I. Vovk, A. Korochkin, A. Neronov and D. Semikoz, *Constraints on the intergalactic magnetic field from Fermi/LAT observations of the 'pair echo' of GRB 221009A*, *Astron. Astrophys.* **683** (2024) A25 [`arXiv:2306.07672`] [INSPIRE].

[23] R. Durrer and A. Neronov, *Cosmological Magnetic Fields: Their Generation, Evolution and Observation*, *Astron. Astrophys. Rev.* **21** (2013) 62 [`arXiv:1303.7121`] [INSPIRE].

[24] T. Vachaspati, *Progress on cosmological magnetic fields*, *Rept. Prog. Phys.* **84** (2021) 074901 [`arXiv:2010.10525`] [INSPIRE].

[25] R. Banerjee and K. Jedamzik, *The Evolution of cosmic magnetic fields: From the very early universe, to recombination, to the present*, *Phys. Rev. D* **70** (2004) 123003 [`astro-ph/0410032`] [INSPIRE].

[26] A. Brandenburg, T. Kahniashvili and A.G. Tevzadze, *Nonhelical inverse transfer of a decaying turbulent magnetic field*, *Phys. Rev. Lett.* **114** (2015) 075001 [`arXiv:1404.2238`] [INSPIRE].

[27] J. Reppin and R. Banerjee, *Nonhelical turbulence and the inverse transfer of energy: A parameter study*, *Phys. Rev. E* **96** (2017) 053105 [`arXiv:1708.07717`] [INSPIRE].

[28] D.N. Hosking and A.A. Schekochihin, *Reconnection-Controlled Decay of Magnetohydrodynamic Turbulence and the Role of Invariants*, *Phys. Rev. X* **11** (2021) 041005 [`arXiv:2012.01393`] [INSPIRE].

[29] D.N. Hosking and A.A. Schekochihin, *Cosmic-void observations reconciled with primordial magnetogenesis*, *Nat. Commun.* **14** (2023) 7523 [`arXiv:2203.03573`] [INSPIRE].

[30] H. Zhou, R. Sharma and A. Brandenburg, *Scaling of the Hosking integral in decaying magnetically dominated turbulence*, *J. Plasma Phys.* **88** (2022) 905880602 [`arXiv:2206.07513`] [INSPIRE].

[31] R. Durrer and C. Caprini, *Primordial magnetic fields and causality*, *JCAP* **11** (2003) 010 [`astro-ph/0305059`] [INSPIRE].

[32] A. Saveliev, K. Jedamzik and G. Sigl, *Time Evolution of the Large-Scale Tail of Non-Helical Primordial Magnetic Fields with Back-Reaction of the Turbulent Medium*, *Phys. Rev. D* **86** (2012) 103010 [`arXiv:1208.0444`] [INSPIRE].

[33] M. Sanati, Y. Revaz, J. Schober, K.E. Kunze and P. Jablonka, *Constraining the primordial magnetic field with dwarf galaxy simulations*, *Astron. Astrophys.* **643** (2020) A54 [`arXiv:2005.05401`] [INSPIRE].

[34] T. Adi, S. Libanore, H.A.G. Cruz and E.D. Kovetz, *Constraining primordial magnetic fields with line-intensity mapping*, *JCAP* **09** (2023) 035 [`arXiv:2305.06440`] [INSPIRE].

[35] J.D. Barrow, P.G. Ferreira and J. Silk, *Constraints on a primordial magnetic field*, *Phys. Rev. Lett.* **78** (1997) 3610 [`astro-ph/9701063`] [INSPIRE].

[36] K. Jedamzik, V. Katalinic and A.V. Olinto, *A Limit on primordial small scale magnetic fields from CMB distortions*, *Phys. Rev. Lett.* **85** (2000) 700 [`astro-ph/9911100`] [INSPIRE].

[37] A. Zizzo and C. Burigana, *On the effect of cyclotron emission on the spectral distortions of the cosmic microwave background*, *New Astron.* **11** (2005) 1 [`astro-ph/0505259`] [INSPIRE].

[38] K.E. Kunze and E. Komatsu, *Constraining primordial magnetic fields with distortions of the black-body spectrum of the cosmic microwave background: pre- and post-decoupling contributions*, *JCAP* **01** (2014) 009 [`arXiv:1309.7994`] [INSPIRE].

[39] K. Subramanian and J.D. Barrow, *Microwave background signals from tangled magnetic fields*, *Phys. Rev. Lett.* **81** (1998) 3575 [`astro-ph/9803261`] [INSPIRE].

[40] K. Subramanian and J.D. Barrow, *Small-scale microwave background anisotropies due to tangled primordial magnetic fields*, *Mon. Not. Roy. Astron. Soc.* **335** (2002) L57 [`astro-ph/0205312`] [INSPIRE].

[41] A. Mack, T. Kahniashvili and A. Kosowsky, *Microwave background signatures of a primordial stochastic magnetic field*, *Phys. Rev. D* **65** (2002) 123004 [`astro-ph/0105504`] [INSPIRE].

[42] A. Lewis, *Observable primordial vector modes*, *Phys. Rev. D* **70** (2004) 043518 [`astro-ph/0403583`] [INSPIRE].

[43] T. Kahniashvili and B. Ratra, *Effects of Cosmological Magnetic Helicity on the Cosmic Microwave Background*, *Phys. Rev. D* **71** (2005) 103006 [`astro-ph/0503709`] [INSPIRE].

[44] G. Chen, P. Mukherjee, T. Kahniashvili, B. Ratra and Y. Wang, *Looking for cosmological Alfven waves in WMAP data*, *Astrophys. J.* **611** (2004) 655 [`astro-ph/0403695`] [INSPIRE].

[45] A. Lewis, *CMB anisotropies from primordial inhomogeneous magnetic fields*, *Phys. Rev. D* **70** (2004) 043011 [`astro-ph/0406096`] [INSPIRE].

[46] H. Tashiro, N. Sugiyama and R. Banerjee, *Nonlinear evolution of cosmic magnetic fields and cosmic microwave background anisotropies*, *Phys. Rev. D* **73** (2006) 023002 [`astro-ph/0509220`] [INSPIRE].

[47] D. Yamazaki, K. Ichiki, T. Kajino and G.J. Mathews, *Constraints on the evolution of the primordial magnetic field from the small scale CMB angular anisotropy*, *Astrophys. J.* **646** (2006) 719 [`astro-ph/0602224`] [INSPIRE].

[48] M. Giovannini, *Entropy perturbations and large-scale magnetic fields*, *Class. Quant. Grav.* **23** (2006) 4991 [`astro-ph/0604134`] [INSPIRE].

[49] T. Kahniashvili and B. Ratra, *CMB anisotropies due to cosmological magnetosonic waves*, *Phys. Rev. D* **75** (2007) 023002 [`astro-ph/0611247`] [INSPIRE].

[50] M. Giovannini and K.E. Kunze, *Magnetized CMB observables: A Dedicated numerical approach*, *Phys. Rev. D* **77** (2008) 063003 [`arXiv:0712.3483`] [INSPIRE].

[51] D.G. Yamazaki, K. Ichiki, T. Kajino and G.J. Mathews, *New Constraints on the Primordial Magnetic Field*, *Phys. Rev. D* **81** (2010) 023008 [`arXiv:1001.2012`] [INSPIRE].

[52] D. Paoletti and F. Finelli, *CMB Constraints on a Stochastic Background of Primordial Magnetic Fields*, *Phys. Rev. D* **83** (2011) 123533 [`arXiv:1005.0148`] [INSPIRE].

[53] J.R. Shaw and A. Lewis, *Constraining Primordial Magnetism*, *Phys. Rev. D* **86** (2012) 043510 [`arXiv:1006.4242`] [INSPIRE].

[54] K.E. Kunze, *CMB anisotropies in the presence of a stochastic magnetic field*, *Phys. Rev. D* **83** (2011) 023006 [`arXiv:1007.3163`] [INSPIRE].

[55] D. Paoletti and F. Finelli, *Constraints on a Stochastic Background of Primordial Magnetic Fields with WMAP and South Pole Telescope data*, *Phys. Lett. B* **726** (2013) 45 [`arXiv:1208.2625`] [INSPIRE].

[56] M. Ballardini, F. Finelli and D. Paoletti, *CMB anisotropies generated by a stochastic background of primordial magnetic fields with non-zero helicity*, *JCAP* **10** (2015) 031 [arXiv:1412.1836] [INSPIRE].

[57] Planck collaboration, *Planck 2015 results. XIX. Constraints on primordial magnetic fields*, *Astron. Astrophys.* **594** (2016) A19 [arXiv:1502.01594] [INSPIRE].

[58] D.R. Sutton, C. Feng and C.L. Reichardt, *Current and Future Constraints on Primordial Magnetic Fields*, *Astrophys. J.* **846** (2017) 164 [arXiv:1702.01871] [INSPIRE].

[59] A. Zucca, Y. Li and L. Pogosian, *Constraints on Primordial Magnetic Fields from Planck combined with the South Pole Telescope CMB B-mode polarization measurements*, *Phys. Rev. D* **95** (2017) 063506 [arXiv:1611.00757] [INSPIRE].

[60] T. Minoda, K. Ichiki and H. Tashiro, *Small-scale CMB anisotropies induced by the primordial magnetic fields*, *JCAP* **03** (2021) 093 [arXiv:2012.12542] [INSPIRE].

[61] S.K. Sethi and K. Subramanian, *Primordial magnetic fields in the post-recombination era and early reionization*, *Mon. Not. Roy. Astron. Soc.* **356** (2005) 778 [astro-ph/0405413] [INSPIRE].

[62] K.E. Kunze and E. Komatsu, *Constraints on primordial magnetic fields from the optical depth of the cosmic microwave background*, *JCAP* **06** (2015) 027 [arXiv:1501.00142] [INSPIRE].

[63] J. Ganc and M.S. Sloth, *Probing correlations of early magnetic fields using mu-distortion*, *JCAP* **08** (2014) 018 [arXiv:1404.5957] [INSPIRE].

[64] J. Chluba, D. Paoletti, F. Finelli and J.-A. Rubiño-Martín, *Effect of primordial magnetic fields on the ionization history*, *Mon. Not. Roy. Astron. Soc.* **451** (2015) 2244 [arXiv:1503.04827] [INSPIRE].

[65] R. Durrer, P.G. Ferreira and T. Kahniashvili, *Tensor microwave anisotropies from a stochastic magnetic field*, *Phys. Rev. D* **61** (2000) 043001 [astro-ph/9911040] [INSPIRE].

[66] T.R. Seshadri and K. Subramanian, *CMBR polarization signals from tangled magnetic fields*, *Phys. Rev. Lett.* **87** (2001) 101301 [astro-ph/0012056] [INSPIRE].

[67] K. Subramanian, T.R. Seshadri and J.D. Barrow, *Small-scale CMB polarization anisotropies due to tangled primordial magnetic fields*, *Mon. Not. Roy. Astron. Soc.* **344** (2003) L31 [astro-ph/0303014] [INSPIRE].

[68] S. Mollerach, D. Harari and S. Matarrese, *CMB polarization from secondary vector and tensor modes*, *Phys. Rev. D* **69** (2004) 063002 [astro-ph/0310711] [INSPIRE].

[69] C. Scoccola, D. Harari and S. Mollerach, *B polarization of the CMB from Faraday rotation*, *Phys. Rev. D* **70** (2004) 063003 [astro-ph/0405396] [INSPIRE].

[70] A. Kosowsky, T. Kahniashvili, G. Lavrelashvili and B. Ratra, *Faraday rotation of the Cosmic Microwave Background polarization by a stochastic magnetic field*, *Phys. Rev. D* **71** (2005) 043006 [astro-ph/0409767] [INSPIRE].

[71] L. Pogosian, T. Vachaspati and A. Yadav, *Primordial Magnetism in CMB B-modes*, *Can. J. Phys.* **91** (2013) 451 [arXiv:1210.0308] [INSPIRE].

[72] T. Kahniashvili, Y. Maravin, G. Lavrelashvili and A. Kosowsky, *Primordial Magnetic Helicity Constraints from WMAP Nine-Year Data*, *Phys. Rev. D* **90** (2014) 083004 [arXiv:1408.0351] [INSPIRE].

[73] L. Pogosian and A. Zucca, *Searching for Primordial Magnetic Fields with CMB B-modes*, *Class. Quant. Grav.* **35** (2018) 124004 [arXiv:1801.08936] [INSPIRE].

[74] I. Brown and R. Crittenden, *Non-Gaussianity from cosmic magnetic fields*, *Phys. Rev. D* **72** (2005) 063002 [`astro-ph/0506570`] [INSPIRE].

[75] T.R. Seshadri and K. Subramanian, *CMB bispectrum from primordial magnetic fields on large angular scales*, *Phys. Rev. Lett.* **103** (2009) 081303 [`arXiv:0902.4066`] [INSPIRE].

[76] C. Caprini, F. Finelli, D. Paoletti and A. Riotto, *The cosmic microwave background temperature bispectrum from scalar perturbations induced by primordial magnetic fields*, *JCAP* **06** (2009) 021 [`arXiv:0903.1420`] [INSPIRE].

[77] R.-G. Cai, B. Hu and H.-B. Zhang, *Acoustic signatures in the Cosmic Microwave Background bispectrum from primordial magnetic fields*, *JCAP* **08** (2010) 025 [`arXiv:1006.2985`] [INSPIRE].

[78] P. Trivedi, K. Subramanian and T.R. Seshadri, *Primordial Magnetic Field Limits from Cosmic Microwave Background Bispectrum of Magnetic Passive Scalar Modes*, *Phys. Rev. D* **82** (2010) 123006 [`arXiv:1009.2724`] [INSPIRE].

[79] I.A. Brown, *Intrinsic Bispectra of Cosmic Magnetic Fields*, *Astrophys. J.* **733** (2011) 83 [`arXiv:1012.2892`] [INSPIRE].

[80] M. Shiraishi, D. Nitta, S. Yokoyama, K. Ichiki and K. Takahashi, *Cosmic microwave background bispectrum of vector modes induced from primordial magnetic fields*, *Phys. Rev. D* **82** (2010) 121302 [*Erratum ibid.* **83** (2011) 029901] [`arXiv:1009.3632`] [INSPIRE].

[81] M. Shiraishi, D. Nitta, S. Yokoyama, K. Ichiki and K. Takahashi, *Cosmic microwave background bispectrum of tensor passive modes induced from primordial magnetic fields*, *Phys. Rev. D* **83** (2011) 123003 [`arXiv:1103.4103`] [INSPIRE].

[82] P. Trivedi, T.R. Seshadri and K. Subramanian, *Cosmic Microwave Background Trispectrum and Primordial Magnetic Field Limits*, *Phys. Rev. Lett.* **108** (2012) 231301 [`arXiv:1111.0744`] [INSPIRE].

[83] M. Shiraishi and T. Sekiguchi, *First observational constraints on tensor non-Gaussianity sourced by primordial magnetic fields from cosmic microwave background*, *Phys. Rev. D* **90** (2014) 103002 [`arXiv:1304.7277`] [INSPIRE].

[84] P. Trivedi, K. Subramanian and T.R. Seshadri, *Primordial magnetic field limits from the CMB trispectrum: Scalar modes and Planck constraints*, *Phys. Rev. D* **89** (2014) 043523 [`arXiv:1312.5308`] [INSPIRE].

[85] R. Banerjee and K. Jedamzik, *Are cluster magnetic fields primordial?*, *Phys. Rev. Lett.* **91** (2003) 251301 [*Erratum ibid.* **93** (2004) 179901] [`astro-ph/0306211`] [INSPIRE].

[86] K. Jedamzik and T. Abel, *Weak Primordial Magnetic Fields and Anisotropies in the Cosmic Microwave Background Radiation*, `arXiv:1108.2517` [INSPIRE].

[87] K. Jedamzik and T. Abel, *Small-scale primordial magnetic fields and anisotropies in the cosmic microwave background radiation*, *JCAP* **10** (2013) 050 [`arXiv:1108.2517`] [INSPIRE].

[88] K. Jedamzik and A. Saveliev, *Stringent Limit on Primordial Magnetic Fields from the Cosmic Microwave Background Radiation*, *Phys. Rev. Lett.* **123** (2019) 021301 [`arXiv:1804.06115`] [INSPIRE].

[89] P.J.E. Peebles, *Principles of Physical Cosmology*, Princeton University Press, Princeton, NJ, U.S.A. (1967) [INSPIRE].

[90] K. Jedamzik and L. Pogosian, *Relieving the Hubble tension with primordial magnetic fields*, *Phys. Rev. Lett.* **125** (2020) 181302 [`arXiv:2004.09487`] [INSPIRE].

[91] K. Jedamzik and L. Pogosian, *Primordial magnetic fields and the Hubble tension*, arXiv:2307.05475 [INSPIRE].

[92] E. Abdalla et al., *Cosmology intertwined: A review of the particle physics, astrophysics, and cosmology associated with the cosmological tensions and anomalies*, *J. High Energy Astrophys.* **34** (2022) 49 [arXiv:2203.06142] [INSPIRE].

[93] L. Thiele, Y. Guan, J.C. Hill, A. Kosowsky and D.N. Spergel, *Can small-scale baryon inhomogeneities resolve the Hubble tension? An investigation with ACT DR4*, *Phys. Rev. D* **104** (2021) 063535 [arXiv:2105.03003] [INSPIRE].

[94] M. Rashkovetskyi, J.B. Muñoz, D.J. Eisenstein and C. Dvorkin, *Small-scale clumping at recombination and the Hubble tension*, *Phys. Rev. D* **104** (2021) 103517 [arXiv:2108.02747] [INSPIRE].

[95] S. Galli, L. Pogosian, K. Jedamzik and L. Balkenhol, *Consistency of Planck, ACT, and SPT constraints on magnetically assisted recombination and forecasts for future experiments*, *Phys. Rev. D* **105** (2022) 023513 [arXiv:2109.03816] [INSPIRE].

[96] M. Lucca, J. Chluba and A. Rotti, *CRRfast: an emulator for the cosmological recombination radiation with effects from inhomogeneous recombination*, *Mon. Not. Roy. Astron. Soc.* **530** (2024) 668 [arXiv:2306.08085] [INSPIRE].

[97] P. Ralegankar, *Dark Matter Minihalos from Primordial Magnetic Fields*, *Phys. Rev. Lett.* **131** (2023) 231002 [arXiv:2303.11861] [INSPIRE].

[98] A. Brandenburg, K. Enqvist and P. Olesen, *Large scale magnetic fields from hydromagnetic turbulence in the very early universe*, *Phys. Rev. D* **54** (1996) 1291 [astro-ph/9602031] [INSPIRE].

[99] S. Naoz and R. Narayan, *Generation of Primordial Magnetic Fields on Linear Over-density Scales*, *Phys. Rev. Lett.* **111** (2013) 051303 [arXiv:1304.5792] [INSPIRE].

[100] N. Lee and Y. Ali-Haïmoud, *Magnetic fields from small-scale primordial perturbations*, *Phys. Rev. D* **109** (2024) 103536 [arXiv:2404.03655] [INSPIRE].

[101] ENZO collaboration, *Enzo: An Adaptive Mesh Refinement Code for Astrophysics*, *Astrophys. J. Suppl.* **211** (2014) 19 [arXiv:1307.2265] [INSPIRE].

[102] P. Wang and T. Abel, *Magnetohydrodynamic Simulations of Disk Galaxy Formation: The Magnetization of The Cold and Warm Medium*, *Astrophys. J.* **696** (2009) 96 [arXiv:0712.0872] [INSPIRE].

[103] P. Anninos, Y. Zhang, T. Abel and M.L. Norman, *Cosmological hydrodynamics with multispecies chemistry and nonequilibrium ionization and cooling*, *New Astron.* **2** (1997) 209 [astro-ph/9608041] [INSPIRE].

[104] T. Abel, P. Anninos, Y. Zhang and M.L. Norman, *Modeling primordial gas in numerical cosmology*, *New Astron.* **2** (1997) 181 [astro-ph/9608040] [INSPIRE].

[105] S. Seager, D.D. Sasselov and D. Scott, *A new calculation of the recombination epoch*, *Astrophys. J.* **523** (1999) L1 [astro-ph/9909275] [INSPIRE].

[106] Y. Ali-Haïmoud and C.M. Hirata, *HyRec: A fast and highly accurate primordial hydrogen and helium recombination code*, *Phys. Rev. D* **83** (2011) 043513 [arXiv:1011.3758] [INSPIRE].

[107] N. Lee and Y. Ali-Haïmoud, *HYREC-2: a highly accurate sub-millisecond recombination code*, *Phys. Rev. D* **102** (2020) 083517 [arXiv:2007.14114] [INSPIRE].

[108] J. Chluba and R.M. Thomas, *Towards a complete treatment of the cosmological recombination problem*, *Mon. Not. Roy. Astron. Soc.* **412** (2011) 748 [`arXiv:1010.3631`] [INSPIRE].

[109] E.E. Kholupenko, A.V. Ivanchik and D.A. Varshalovich, *Rapid He II → He I recombination and radiation concerned with this process*, *Mon. Not. Roy. Astron. Soc.* **378** (2007) 39 [`astro-ph/0703438`] [INSPIRE].

[110] P.J.E. Peebles, *Recombination of the Primeval Plasma*, *Astrophys. J.* **153** (1968) 1 [INSPIRE].

[111] S. Seager, D.D. Sasselov and D. Scott, *How exactly did the universe become neutral?*, *Astrophys. J. Suppl.* **128** (2000) 407 [`astro-ph/9912182`] [INSPIRE].

[112] W.Y. Wong, A. Moss and D. Scott, *How well do we understand cosmological recombination?*, *Mon. Not. Roy. Astron. Soc.* **386** (2008) 1023 [`arXiv:0711.1357`] [INSPIRE].

[113] D. Pequignot, P. Petitjean and C. Boisson, *Total and effective radiative recombination coefficients*, *Astron. Astrophys.* **251** (1991) 680.

[114] L. Senatore, S. Tassev and M. Zaldarriaga, *Cosmological Perturbations at Second Order and Recombination Perturbed*, *JCAP* **08** (2009) 031 [`arXiv:0812.3652`] [INSPIRE].

[115] N. Lee and Y. Ali-Haïmoud, *Probing small-scale baryon and dark matter isocurvature perturbations with cosmic microwave background anisotropies*, *Phys. Rev. D* **104** (2021) 103509 [`arXiv:2108.07798`] [INSPIRE].

[116] T. Venumadhav and C. Hirata, *Stability of small-scale baryon perturbations during cosmological recombination*, *Phys. Rev. D* **91** (2015) 123009 [`arXiv:1409.1240`] [INSPIRE].

[117] Y. Ali-Haïmoud, D. Grin and C.M. Hirata, *Radiative transfer effects in primordial hydrogen recombination*, *Phys. Rev. D* **82** (2010) 123502 [`arXiv:1009.4697`] [INSPIRE].

[118] C.M. Hirata, *Two-photon transitions in primordial hydrogen recombination*, *Phys. Rev. D* **78** (2008) 023001 [`arXiv:0803.0808`] [INSPIRE].

[119] C.M. Hirata and J. Forbes, *Lyman-α transfer in primordial hydrogen recombination*, *Phys. Rev. D* **80** (2009) 023001 [`arXiv:0903.4925`] [INSPIRE].

[120] D. Paoletti, J. Chluba, F. Finelli and J.A. Rubino-Martin, *Improved CMB anisotropy constraints on primordial magnetic fields from the post-recombination ionization history*, *Mon. Not. Roy. Astron. Soc.* **484** (2019) 185 [`arXiv:1806.06830`] [INSPIRE].

[121] D. Paoletti, J. Chluba, F. Finelli and J.A. Rubiño-Martin, *Constraints on primordial magnetic fields from their impact on the ionization history with Planck 2018*, *Mon. Not. Roy. Astron. Soc.* **517** (2022) 3916 [`arXiv:2204.06302`] [INSPIRE].

[122] P. Trivedi, J. Reppin, J. Chluba and R. Banerjee, *Magnetic heating across the cosmological recombination era: Results from 3D MHD simulations*, *Mon. Not. Roy. Astron. Soc.* **481** (2018) 3401 [`arXiv:1805.05315`] [INSPIRE].

[123] A.G. Kritsuk et al., *Comparing Numerical Methods for Isothermal Magnetized Supersonic Turbulence*, *Astrophys. J.* **737** (2011) 13 [`arXiv:1103.5525`] [INSPIRE].

[124] M. Dijkstra, *Physics of the Hydrogen Lyman-alpha radiation transfer*, in *Lyman-alpha as an astrophysical and cosmological tool*, talk given at the *46th "Saas-Fee Advanced Course" of the Swiss Society for Astrophysics and Astronomy (SSAA)*, Les Diablerets, Switzerland, 13–19 March 2016, `arXiv:1704.03416` [INSPIRE].